Materials Science & Engineering A 939 (2025) 148417

Contents lists available at ScienceDirect

Materials Science & Engineering A

journal homepage: www.elsevier.com/locate/msea

Ni-based superalloy 718 fabricated by arc-based directed energy deposition: an experimentally-based strengthening mechanisms analysis

Francisco Werley Cipriano Farias [a,b,*], Valdemar Rebelo Duarte [a,c], João da Cruz Payão Filho [b], Arthur Ribeiro Figueiredo [b], Norbert Schell [d], Emad Maawad [d], Fabio Machado Alves da Fonseca [e], Jonathan Cormier [e], Antonio J. Ramirez [f], Telmo G. Santos [a,c], J.P. Oliveira [a,g,**]

[a] UNIDEMI, Department of Mechanical and Industrial Engineering, NOVA School of Science and Technology, Universidade NOVA de Lisboa, 2829-516, Caparica, Portugal
[b] Program of Metallurgical and Materials Engineering, Federal University of Rio de Janeiro (UFRJ), CEP 21941-972, Rio de Janeiro, RJ, Brazil
[c] Laboratório Associado de Sistemas Inteligentes, LASI, 4800-058, Guimarães, Portugal
[d] Helmholtz-Zentrum Hereon, Institute of Materials Physics, Max-Planck-Str. 1, Geesthacht, 21502, Germany
[e] Institut Pprime, UPR CNRS 3346, Physics and Mechanics of Materials Department, ISAE-ENSMA, 1 Avenue Clément Ader, Futuroscope, Chasseneuil, BP 40109, 86961, France
[f] Ohio State University – Department of Materials Science and Engineering, Columbus, OH, USA
[g] CENIMAT|i3N, Department of Materials Science, School of Science and Technology, NOVA University, Lisbon, Caparica, Portugal

ARTICLE INFO

Keywords:
Inconel 718
Additive manufacturing
Directed energy deposition
Wire and arc additive manufacturing
Strengthening mechanism

ABSTRACT

The present work describes and quantitatively assesses the strengthening mechanisms in Inconel 718 fabricated by arc-based DED (IN718 arc-based DED) through an experimentally-based approach. IN718 arc-based DED (in the as-built condition) showed a typical coarse (millimetric-sized grains) and oriented (cube texture) microstructure with a significant quantity of interdendritic eutectics (Laves and MC-type carbides). After heat treatment (1100 °C/2 h + aging), these eutectics were partially dissolved; however, the original grain size and crystallographic texture aspects were not altered. In addition, the heat treatment promoted a notorious γ″ (Ni_3Nb) and γ′ (Ni_3(Al, Ti)) phases content (~17 and 5 %, respectively), which results in superior room temperature tensile strength despite the aforementioned non-optimized microstructure. The grain size, dislocation density, precipitation content and morphology, and alloying elements in solid solution were experimentally measured and utilized as input data for a quantitative assessment of the strengthening mechanisms. This analysis concludes that the linear dependence of the majority of the strengthening mechanisms on the Taylor factor predominantly promoted the yield strength anisotropy. Furthermore, as expected, it is evidenced that the precipitation strengthening mechanism governs the final strength of IN718 arc-based DED.

1. Introduction

Ni-based superalloy 718 (UNS 07718; commercially known as Inconel 718 – IN718) is a precipitation-strengthened alloy (γ matrix; cubic; Fm $\bar{3}$ m) primarily hardened by the metastable and coherent γ″ (Ni_3Nb; $D0_{22}$; tetragonal; I4/mmm) and stable and coherent γ′ (Ni_3(Al, Ti); cubic; $L1_2$; Pm $\bar{3}$ m) phases [1]. The γ″ phase is the main hardening phase due to its higher volume content (~13–17 %) compared to γ′ (~5 %) [2–4]. The strengthening efficiency of γ′ and γ″ phases depends on their size, volume fraction, and the strain (mismatch) induced at the (semi)coherent interfaces [5], which are related to the primary microstructure (processing condition, e.g., cast and wrought) and heat treatments [3,6,7]. Additionally, IN718 is also strengthened by solid solution (elastic field induced by alloying elements, e.g., Fe, Nb, Al, and Mo),

* Corresponding author. UNIDEMI, Department of Mechanical and Industrial Engineering, NOVA School of Science and Technology, Universidade NOVA de Lisboa, 2829-516, Caparica, Portugal.
** Corresponding author. UNIDEMI, Department of Mechanical and Industrial Engineering, NOVA School of Science and Technology, Universidade NOVA de Lisboa, 2829-516, Caparica, Portugal.
E-mail addresses: fw.farias@campus.fct.unl.pt, werleyfarias@metalmat.ufrj.br (F.W.C. Farias), jp.oliveira@fct.unl.pt (J.P. Oliveira).

https://doi.org/10.1016/j.msea.2025.148417
Received 23 November 2024; Received in revised form 5 March 2025; Accepted 28 April 2025
Available online 29 April 2025
0921-5093/© 2025 The Authors. Published by Elsevier B.V. This is an open access article under the CC BY license (http://creativecommons.org/licenses/by/4.0/).

grain boundaries (grain size), and dislocation density (strain hardening) strengthening mechanisms [8,9]. However, as emphasized by Rielli et al. [10], these mechanisms for wrought IN718 in heat-treated condition (solution + aging) are secondary compared to the precipitation strengthening (i.e., γ' and γ'').

Upon the primary dependence of the final strength of IN718 on the γ' and γ'' content and their morphological aspects, when processing this alloy thought the traditional fusion-based processes (e.g., welding and casting), it is typically observed an inferior room temperature strength in relation to the wrought IN718 [11–22]. This is attributed to significant Nb (γ''-former element) segregation to the interdendritic region and the Nb-rich eutectics precipitation (e.g., Laves phase and MC-type carbides) during the IN718 solidification. The non-homogeneous distribution of Nb also promotes a heterogeneous distribution of γ'' and different precipitation kinetics in the dendritic core and interdendritic regions [15,16]. These aspects become more critical for IN718 fabricated by additive manufacturing (AM), especially in processes with low-energy density (e.g., arc-based directed energy deposition, arc-based DED). The layer-by-layer process fashion of AM continuously alters the thermal boundary conditions (i.e., solidification), leading to different segregation patterns throughout the part [23]. Additionally, IN718 fabricated by arc-based DED is characterized by a non-optimized microstructure, with coarse (millimeter-sized) and cube (<100>{100}) textured grains [16,24–26], in comparison to wrought material (fine and non-oriented equiaxed grains) [27,28]. These characteristics, along with Nb heterogenous distribution, compromise the mechanical behavior and justify the lower performance of IN718 arc-based DED [11–22], demanding the development of dedicated in-process microstructure refinement (e.g., thermal management, interlayer mechanical deformation, and vibration-assisted deposition) and/or post-processing procedures (e.g., heat treatment and hot isostatic pressure) [29–31].

The (semi)quantitative description of the strengthening mechanisms and tensile behaviour of traditionally manufactured IN718 is well-documented [10,32–38]; however, a similar comprehensive approach for additively manufactured IN718 (e.g., IN718 arc-based DED) is still lacking. Sui et al. [39] and Sun et al. [40] ranked the influence of the aforementioned strengthening mechanisms on IN718 fabricated by laser-based DED. They obtained a good agreement between the estimated and experimentally measured yield strength, demonstrating that precipitation (i.e., γ' and γ'') is the primary strengthening mechanism for additively manufactured IN718. This finding is in accordance with the (semi)quantitative description for traditionally manufactured IN718 [10,32–38]. However, these authors [39,40] considered a Taylor factor similar to that of non-oriented materials (~3.06), which does not physically correspond to the Taylor factor observed for additively manufactured materials with cube texture orientation (~2.4–2.8) [26,41–43]. In addition, Zhang et al. [44] pointed out, through a (semi) quantitative description of the strengthening mechanisms, that the effects of eutectics (Laves and MC-type carbides) on the final strength of IN718 fabricated by laser powder bed fusion (PBF) are not significant, a finding that was also verified for IN718 arc-based DED (coarse incoherent eutectics) [26]. Despite several works focused on IN718 fabricated by arc-based DED [11–22], to the best of the authors' knowledge, only Farias et al. [26] have performed a semi-quantitative analysis of the strengthening mechanisms. They observed that, using a specially developed heat treatment, it is possible to induce a similar hardening phase content to that of PBF and wrought material, counterbalancing the deleterious effects of a coarse and oriented microstructure on the tensile behavior. However, it is worth mentioning that the analysis performed by Farias et al. is based on both a literature- and experimental-informed description, which may not fully represent the physical and microstructural aspects related to the strengthening mechanisms in IN718 arc-based DED.

Despite the numerous studies on IN718 arc-based DED [11–22], a clear correlation between the microstructure and tensile behavior of IN718 arc-based DED has not been established. This is particularly relevant for explaining the lower ultimate tensile strength and the anisotropy, which may hinder the use of IN718 arc-based DED in mission-critical applications (e.g., energy and aviation industries). In other words, IN718 arc-based DED fails to meet rigorous requirements (e.g., AMS 5662 and API 20S). To the best of the authors' knowledge, the observed behavior is superficially attributed to the lower energy density of arc-based DED (lower cooling rate in relation to other fusion-based AM processes) without considering critical microstructural factors (grain size and stereology, crystallographic texture, volume fraction of second phases, …). Moreover, the (semi)quantitative strengthening mechanism approaches previously mentioned [26,39,40,44] are based on those developed for traditionally manufactured IN718 [10,32–38], which have shown suitable agreement with experimental results for additively manufactured IN718. However, each metal AM category (e.g., PBF and DED) and sub-category (e.g., laser- and arc-based DED) can originate specific microstructure-property relationships that are not yet fully understood. In this regard, the present work aims to describe and quantitatively assess the tensile behavior of Inconel 718 fabricated by arc-based DED through an experimentally-based procedure. For this purpose, single-bead multi-layer parts were 3D printed and characterized using optical microscopy (OM), scanning electron microscopy (SEM), electron backscatter diffraction (EBSD), transmission electron microscopy (TEM), and synchrotron X-ray diffraction (SXRD). Additionally, the mechanical behavior was evaluated through uniaxial tensile testing.

2. Materials and methods

2.1. Sample fabrication

Single-bead multi-layer parts ($7 \times 55 \times 120$ mm^3) were printed using an in-house developed arc-based DED 3D printer. This printer is composed of two main sections: (i) a semi-automatic gas metal arc (GMA) welding machine (Oerlikon® CITOWAVE III 520) and (ii) a 3-axis computer numerical control (CNC) positioner [45]. The feedstock material (UNS N07718; 1.2 mm; voestalpine Böhler Welding; Table 1) was consolidated on a hot-rolled C-Mn steel plate. Table 2 depicts the printing parameters used to obtain defect-free parts.

Following deposition, the sample was subjected to the mandatory post-deposition heat treatment, which consisted of two stages: (i) homogenization (1100 °C/2 h) and (ii) aging (718 °C/8 h, cooling to 621 °C, and holding at 621 °C/8 h). The heat treatment was designed based on the typical heat treatment used for cast Inconel 718 (AMS 5383 standard). However, the solution step was omitted to prevent the δ phase precipitation. For details regarding the considerations involved in selecting the soaking time and omitting the solution step, refer to our previous work [26].

2.2. Materials characterization

OM (Leica DM IRM) and SEM (Thermo Scientific Quattro) samples were prepared following the standard metallographic procedure (i.e., grinding and polishing), followed by electrolytic etching (10 wt% oxalic acid in water, 6 V for 25 s). Samples for EBSD (EDAX Velocity camera) underwent an additional polishing step on a vibratory polisher (Vibro-Met®; SiO_2; 0.04 μm; 2 h). The step size, voltage, and tilt angle used in EBSD analyses were 1 μm, 20 kV, and 70°, respectively. EBSD data post-processing was carried out using the MTEX-Toolbox [46].

TEM foils were prepared using a focused ion beam SEM (Helios NanoLab 600 DualBeam, FEI) and then cleaned using a Fischione Nanomill. High-angle-annular dark-field (HAADF) TEM images were captured in a Titan3™ G2 60–300 S/TEM (300 kV) coupled with energy-dispersive X-ray spectroscopy (Super-X EDS detector, Thermo Scientific).

The high-energy SXRD (0.14235 Å) was performed at HEMS beamline of PETRA III/DESY. The raw data (2D Debbye-Scherrer diffraction

Table 1
– Feedstock material chemical composition (weight %).

	Ni	Cr	Fe	Nb	Mo	Ti	Al	C	Mn	Si	P	S
Nominal composition	52.52	17.41	20.23	5.25	2.98	0.98	0.45	0.05	0.04	0.08	0.002	0.001
AWS A5.14 ERNiFeCr-2	50–55	17–21	Bal.	4.75–5.5	2.8–3.3	0.65–1.15	0.2–0.8	0.08	0.35	0.35	0.015	0.015
AMS 5383							0.4–0.8					
API 6ACRA				4.87–5.2		0.80–1.15	0.4–0.6	0.045	0.35	0.35	0.01	0.01

Table 2
– Arc-based DED 3D printing parameters.

Current[a]	137 [A]
Tension[a]	17 [V]
Wire feed speed	4 [m/min]
Travel speed	5 [mm/s]
Heat input[b]	372.6 [J/mm]
Interlayer temperature	150 [°C]
Contact-tip-to-work distance	12 [mm]
Shielding gas specification	AWS A5.32
Shielding gas	I3 – ArHe −25
Shielding gas flow	15 [l/min]
Substrate preparation	ISO 8501-1

[a] Root mean square (RMS).
[b] Thermal efficiency (η = 0.8), BS EN 1011-1.

rings) were post-processed using FIT2D [47]. For experimental setup details, refer to our previous works [30,48]. Additionally, the content of the hardening phase was estimated using the Rietveld refinement (DIFFRAC.TOPAS software, Bruker). For details about the Rietveld refinement, see the Supplementary Material.

2.3. Tensile test

Tensile tests at room temperature were conducted on cylindrical specimens (Supplementary Material) extracted both perpendicular (horizontal) and parallel (vertical) to the building direction. These specimens were fabricated by electric discharge machining, followed by turning and low-stress mechanical polishing to remove machining-induced work hardening and surface scratches. The tensile tests were performed at a strain rate of 5.0×10^{-4} s^{-1} using an Instron® 8562 machine equipped with a 100 kN load cell and a contact extensometer. The engineering stress-strain curves were analyzed in accordance with ASTM E8 standard. Three specimens were evaluated for each condition.

2.4. Thermodynamic simulations

Thermodynamic simulations were used to support the microstructural characterization. The Scheil–Gulliver model, which considers back diffusion, with carbon fast diffusion enabled, and a cooling rate of 10^2 °C/s [49,50], was conducted using the Thermo-Calc® software (TCNI11 and MOBNI5 databases). The chemical composition (Table 1) and the phases identified in SXRD were used as input data.

3. Results and discussion

3.1. Microstructural characterization

Fig. 1 depicts the microstructure of the IN718 DED (as-built and heat-treated conditions). In both conditions, it is possible to identify coarse and aligned grains parallel to the building direction, which reveals that the heat treatment did not alter the primary grain microstructure. In the

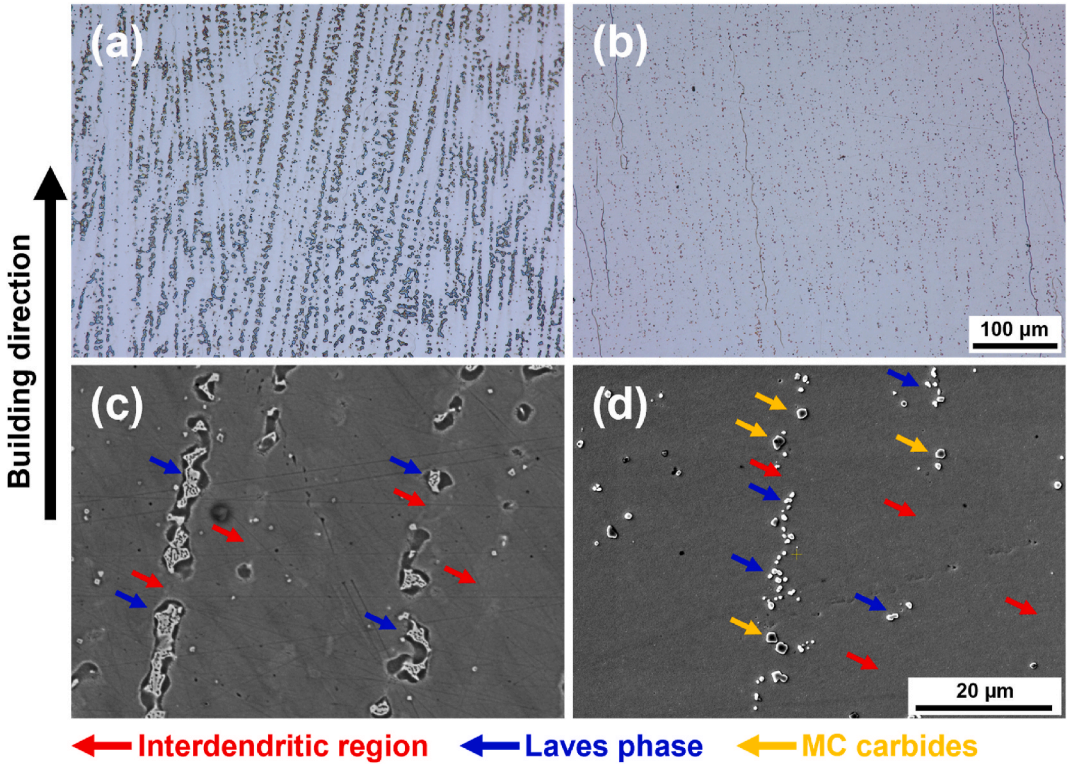

Fig. 1. – Optical and scanning electron microscopy of Inconel 718 fabricated by arc-based directed energy deposition: (a) and (c) as-built and (b) and (d) heat-treated conditions.

interdendritic region, it is observed the eutectics, which are not completely dissolved after the heat treatment, presenting a dotted pattern (heat-treated) instead of a continuous long-chain (as-built) [39,51]. These eutectics were classified based on their chemical composition and morphology (Fig. 2), as well as crystallographic aspects (Fig. 3), into Laves phase and MC-type carbides. The identified eutectics are in accordance with the solidification sequence proposed by DuPont et al. [52] (Nb-bearing Ni-based superalloys welded) and indicated by the Schiel-Gulliver model (Fig. 4), as well as experimentally verified by Oh et al. [53] (*in situ* SXRD during solidification of IN718 laser-based DED). The as-built condition (Fig. 2) also shows the formation of the δ phase near the Nb-rich zones (Laves phase at the interdendritic zone), which is associated with the multiple thermal cycles and the high precipitation kinetics in the Nb-rich zones [23,26]. Moreover, Fig. 4b also indicates that the δ phase can be part of the solidification sequence, which was corroborated by Oh et al. [53].

Fig. 2 also reveals that the "MC-type carbides" are composed of a core-shell structure with three layers (from internal to external): (i) Al-based oxide, (ii) Ti-rich MC-type carbide, and (iii) Nb-rich MC-type carbide. This type of morphology has been previously reported for Inconel 625 (weld cladding) [54,55] and Inconel 718 (additive manufacturing) [56,57]. The authors believe that Al-oxide formation is associated with oxygen pick-up during part deposition, as previously indicated by Xu et al. [11] and Zhang et al. [58]. The layer just deposited and its adjacent area (still incandescent) reacted with the oxygen present in the atmosphere (regions not fully protected by the shielding gas), creating an oxide scale that will be remelted during the subsequent layer deposition, thereby increasing the oxygen content in the melting pool. Consequently, according to the Ellingham–Richardson diagram [59,60], Al tends to react rapidly with oxygen. Thus, Al-oxide (core) forms before MC-type carbides (shell), which use the Al-oxides as nucleation sites, leading to the formation of the aforementioned core-shell structure. After the homogenization heat treatment, the solid-state precipitated phases (δ, γ″, and γ′) dissolved due to the high peak temperature and prolonged soaking time (1100 °C for 2 h), leaving only the undissolved eutectics, as demonstrated in Figs. 1 and 3. This is in accordance with the equilibrium diagram (Fig. 4a), which shows that the δ, γ″, and γ′ phases are unstable at 1100 °C. In addition, the heat treatment induces a partial dissolution of the eutectics (especially Laves phase, which changes its morphology), as confirmed by the vanishing or reduced peak intensity in the SXRD (Fig. 3). However, a significant quantity of eutectics remains (Fig. 1), particularly MC-type carbides, which are stable at the heat treatment temperature [17,18,26].

In relation to crystallographic aspects (refer to pole figures, Fig. 5a and b), as mentioned earlier (Fig. 1), the heat treatment is unable to alter the coarse and oriented grains usually observed in IN718 arc-based DED [11–22]. As a result, the heat-treated material continues to exhibit the characteristic cube texture commonly observed in face-centered cubic

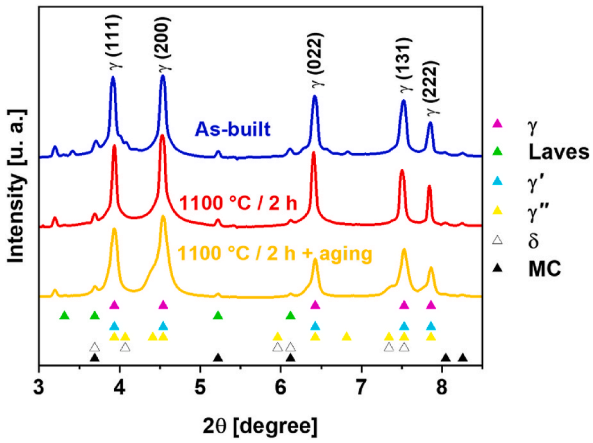

Fig. 3. – Synchrotron X-ray diffraction of the Inconel 718 fabricated by arc-based directed energy deposition (as-built and heat-treated conditions). The symbol * represents a represents a second harmonic peak.

(FCC) materials processed by fusion-based techniques (e.g., welding, casting, and additive manufacturing) [16,24–26]. This observation is further supported by the presence of the highest intensity (200) peak in SXRD (Fig. 3), i.e., volumetric evidence of texture aspects. The cube texture observed in fusion-based processed non-transformable alloys, such as Inconel 718, arises from competitive growth and a nearly unidirectional heat flux, which promotes dendrite growth almost perpendicular to the fusion line [61,62]. In addition, for FCC materials, the planes and directions with the lowest planar and linear densities, {100} and <100>, respectively, grow faster than other directions [63–65]. Thus, cube-textured grains aligned with the maximum thermal gradient will impinge the growth of remaining grains (competitive growth) and induce a non-randomized microstructure in the melting pool [66]. Additionally, due to the layer-by-layer deposition fashion of arc-based DED, each subsequent layer partially remelts the previous one and solidifies from it, maintaining the same crystallographic orientation, a procedure known as epitaxial growth [67]. Thus, layer by layer, the cube texture in the newly deposited layers intensifies [68], becoming dominant in medium to large-sized parts [69].

The crystallographic texture was also related to the Taylor factor (*M*, Fig. 5c and d) [70,71]. *M* refers to the susceptibility of each grain in a polycrystalline aggregate to accommodate the deformation induced by dislocation sliding, considering that all grains undergo similar deformation [72]. Therefore, depending on the stress (e.g., vertical and horizontal tensile tests) and grain orientations, a specific grain can be more (soft grain, lower M) or less (hard grain, higher M) susceptible to deformation. Hosford [70] performed several calculations for *M*, considering distinct crystallographic orientations and stress states. For

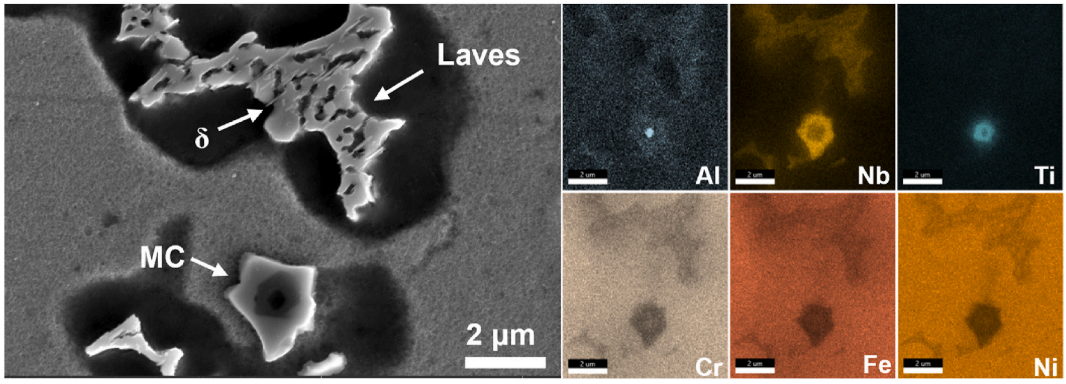

Fig. 2. – High-resolution scanning electron microscopy image and energy-dispersive X-ray spectroscopy of the Inconel 718 fabricated by arc-based directed energy deposition (as-built condition).

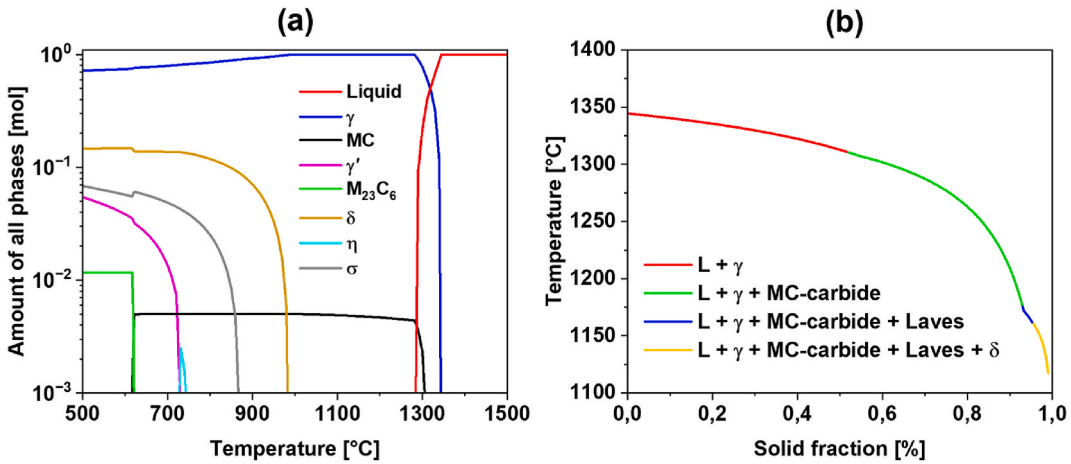

Fig. 4. – (a) Equilibrium and (b) Scheil-Gulliver solidification diagrams of Inconel 718.

ideally cube-oriented wires (aligned grains with <100> fiber textures) loaded along the wire axis of symmetry, M was estimated to be equal to $\sqrt{6} \approx 2.45$. Therefore, considering the typical microstructure observed for IN718 arc-based DED (<100>{100} texture, Fig. 5), M must be around that presented by wires with ideal <100> fiber textures, which was experimentally confirmed (2.7 ± 0.15 and 2.47 ± 0.07,Fig. 5c and d). The higher M (2.7) in relation to wires with ideal <100> fiber texture was related to the non-ideal texture observed for IN718 arc-based DED parallel to the building direction, i.e., grains not perfectly aligned with the build direction [73]. Additionally, for samples analyzed transversely to the building direction, M (2.47 ± 0.07) was almost identical to the ideally calculated M (2.45). Therefore, according to Liang et al. [41] (Hastelloy X fabricated by laser-based DED) and Thijs et al. [74] (Ta alloy X fabricated by laser-based PBF), samples tested in the horizontal direction (transverse to the building direction, M = 2.47 ± 0.07) are expected to be less resistant to deformation than those tested in the vertical direction (M = 2.7 ± 0.15). It is worth noting that, due to the coarse grain size, M in the present work was estimated using a weighted average that accounted for the M of each grain and its respective area, such as proposed by Thijs et al. [74].

Finally, in order to analyze the aged material, a transmission electron microscopy analysis (Fig. 6) was performed to support the SXRD data (Fig. 3). The γ′ (Ni_3(Al, Ti)) and γ″ (Ni_3Nb) phases were distinguished by their chemical composition and morphology (sphere/cubic and lens like disk shape, respectively [75,76]). According to Cozar and Peinau [77] and Theska et al. [33], in wrought Inconel 718 direct aged (i.e., without solution heat treatment, as in the present work), the typical precipitate morphologies observed were γ′ and γ″ (monolith), γ′-γ″ duplets and γ″-γ′-γ″ triplets (sandwich like structure). Additionally, Rielli et al. [76] also observed these precipitate morphologies in IN718 fabricated by PBF (direct aged). In the present work (Figs. 6 and 7), γ″ and γ′ (monoliths), γ′-γ″ doublets, and γ″-γ′-γ″ triplets were also confirmed, which indicates that these precipitate morphologies can also occur across different processing routes, such as forging, PBF, and DED. In addition, the duplets and triplets suggest that γ″ precipitates first, followed by γ′ [78], which is in accordance with the differential scanning calorimetry study performed by Semiatin et al. [79]. Shi et al. [80] reported that, during the aging heat treatment, the precipitation of γ″ and γ′ rejected Al and Nb for adjacent regions, respectively. Rielli et al. [81] demonstrated that the precipitation of γ″ in Nb-rich zones occurred more easily for the direct aging condition. Thus, as the γ″ precipitation rejects Al (i.e., its adjacent regions become enriched in γ′-forming elements), it can act as a heterogeneous nucleus for γ′ (pre-existing surfaces and Al-rich regions), which may explain the formation of a significant fraction of γ′-γ″ duplets and even γ″-γ′-γ″ triplets.

The γ′ and γ″ particle sizes (Fig. 6 and Supplementary Material) were estimated based on the chemical composition distribution. The measured particles sizes for γ′ and γ″ (~11.62 ± 1.67 and 17.02 ± 3.3 nm, respectively) were in accordance with those estimated experimentally by Rielli et al. [76,81] (atom probe), Sui et al. [39] (TEM), Slama et al. [82] (TEM), and Devaux et al. [83] (TEM). Geng et al. [78] reported that the Al enrichment (Fig. 7) during γ″ precipitation stabilizes the interface between γ″ and γ′ and hinders the assimilation of Nb from γ′ to γ″ (i.e., γ″ tends to grow only from one side), which maintains the precipitate particle size fine even during long aging heat treatments and/or service operations. Moreover, the γ″ thickness (e, 6.1 ± 1.5 nm) and particle size ($2R_{\gamma''}$, Fig. 6b) followed the correlation established by Sui et al. [39] (literature survey), which deduced a linear relationship between $2R_{\gamma''}$ and e ($2R_{\gamma''} = 4.5026e - 9.649$) for additively manufactured and wrought Inconel 718.

The hardening phase content was estimated using TEM/EDS (Fig. 6) analysis and compared with the Rietveld refinement of the SXRD data (Table 3), which demonstrated a good agreement (γ″ – 17.02 % vs.17.39 % – and γ′ – 5.01 % vs. 4.15 %, respectively). This suggests that the Rietveld refinement applied to synchrotron X-ray diffraction can satisfactorily estimate the hardening phase content, as also demonstrated by Ferreri et al. [2] and Smith et al. [75]. Additionally, the volume fraction of the hardening phases estimated by TEM/EDS and SRXD is in accordance with the literature data for Inconel 718 processed in several conditions (e.g., cast, forging, and powder bed fusion) [2–4,32,39,44,76,81,84]. These results reinforce the suitability of the developed heat treatment for IN718 arc-based DED [26], indicating that despite the non-optimized microstructure (Nb segregation and coarse grain size), a significant hardening phase content can be achieved through an appropriate selection of soaking time and homogenization peak temperature (i.e., a maximum dissolution of eutectics).

3.2. Tensile testing

The IN718 arc-based DED showed a usual strain × stress curve with a clear ductile behavior (Fig. 8), characterized by a fracture surface composed of dimples (Fig. 9), i.e., the failure mode was the coalescence of microcavities [85]. In addition, the horizontal specimen (Fig. 9a) showed a 'dendrite solidification pattern' on the fracture surface, which is associated with the incoherent eutectic (interdendritic zone) that acts as a dimple nucleation site [39,86]. Subsequently, these dimples grow and coalesce, generating the previously mentioned patterns. The yield strength, *YS*, and ductility requirements of AMS 5662 were met using the typical process route (AM + heat treatment). However, the ultimate tensile strength, *UTS*, requirement was not met, similar to what has been previously observed in the literature [15–18]. This aligns with the lower strain-hardening exponent (0.0945 and 0.1123 for horizontal and

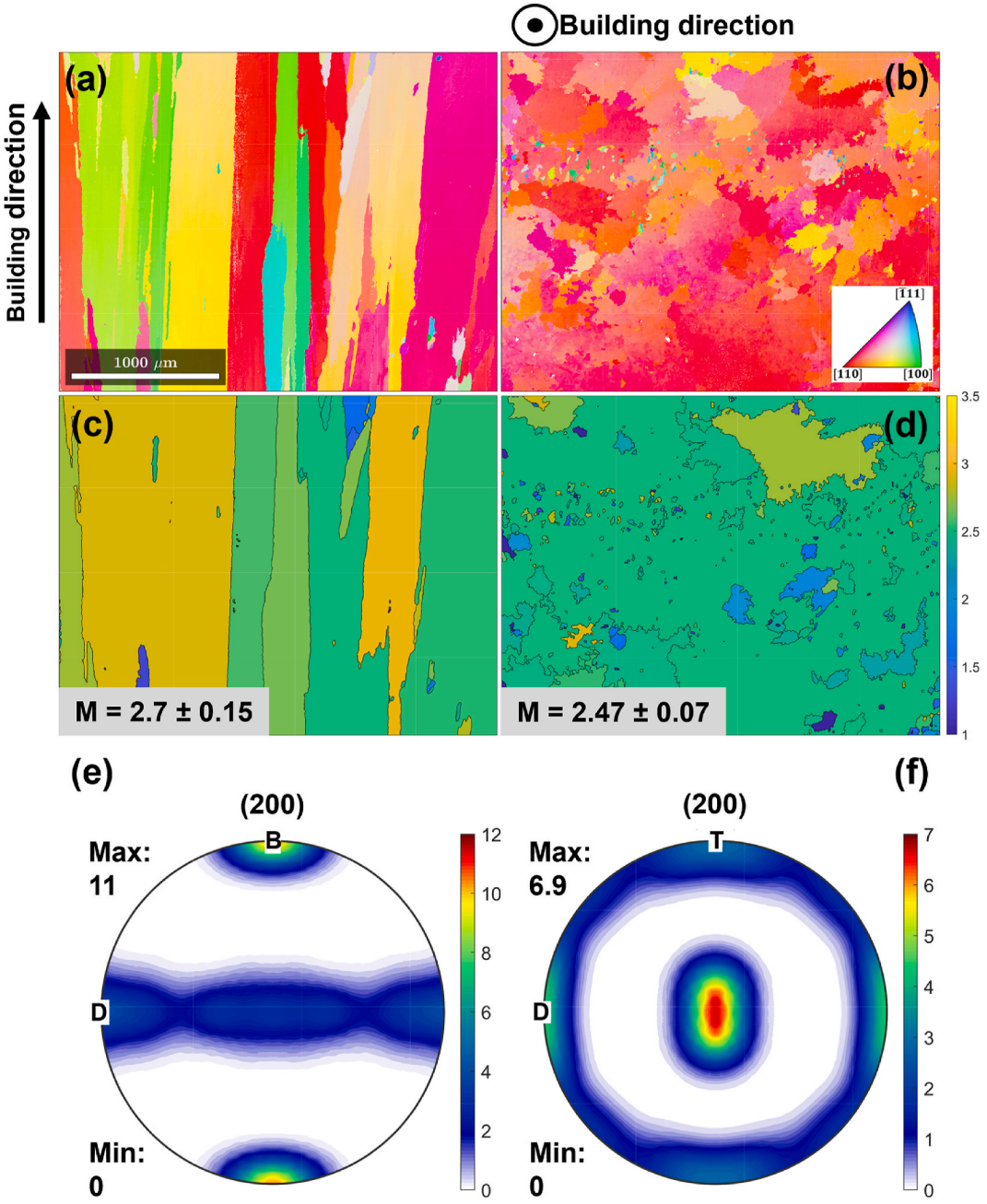

Fig. 5. – EBSD analysis of the Inconel 718 fabricated by arc-based directed energy deposition (heat-treated condition): (a) and (b) orientation image map, (c) and (d) Taylor factor maps, and (e) and (f) pole figures. In (e) and (f), B, D, and T represent building, deposition, and transversal directions, respectively.

vertical, respectively), a typical aspect observed in coarse-grainsized materials [87,88]. The strain-hardening exponent, *n*, was estimated by fitting the strain-stress curve using a Holleman's-type power law equation [89]. Additionally, Table 4 compares the present results with those from the literature, demonstrating that the selected heat treatment promoted superior mechanical properties in relation to the majority of available data. These results were primarily attributed to the higher hardening phases content (refer to Table 3). Finally, the IN718 arc-based DED fully met the requirements of cast (AMS 5383) and PBF (ASTM F3055) materials, reinforcing that arc-based DED can achieve tensile properties comparable to those observed in several conventional process routes (e.g., forging, welding, and casting) through a properly designed heat treatment.

Keller et al. [94], based on the Kocks-Mecking model [95], described that the increase in dislocation density during tensile testing at room temperature (i.e., the strain-hardening) is mainly dependent on *M* (directly proportional), the mean free path of gliding dislocations (inversely and non-linearly proportional to grain size [96]), the generation rate of geometrically necessary dislocations (inversely proportional to grain size [97]), and the initial dislocation structures (directly proportional). Therefore, considering that the IN718 arc-based DED exhibited a smaller *M* (Fig. 5) compared to a non-oriented and equiaxed material (~3.06) [70,71], a larger grain size (refer to Section 3.3.2), and a lower initial dislocation density (heat-treated condition, refer to Section 3.3.3), the notably lower strain-hardening exponent of IN718 arc-based DED (0.0945 and 0.1123) compared to wrought material (~0.5–0.7) [98] can be justified. Furthermore, following the same rationale, it was expected that the vertical specimens would have a slightly higher strain-hardening exponent (higher *M*) compared to the horizontal direction, which was verified experimentally. Therefore,

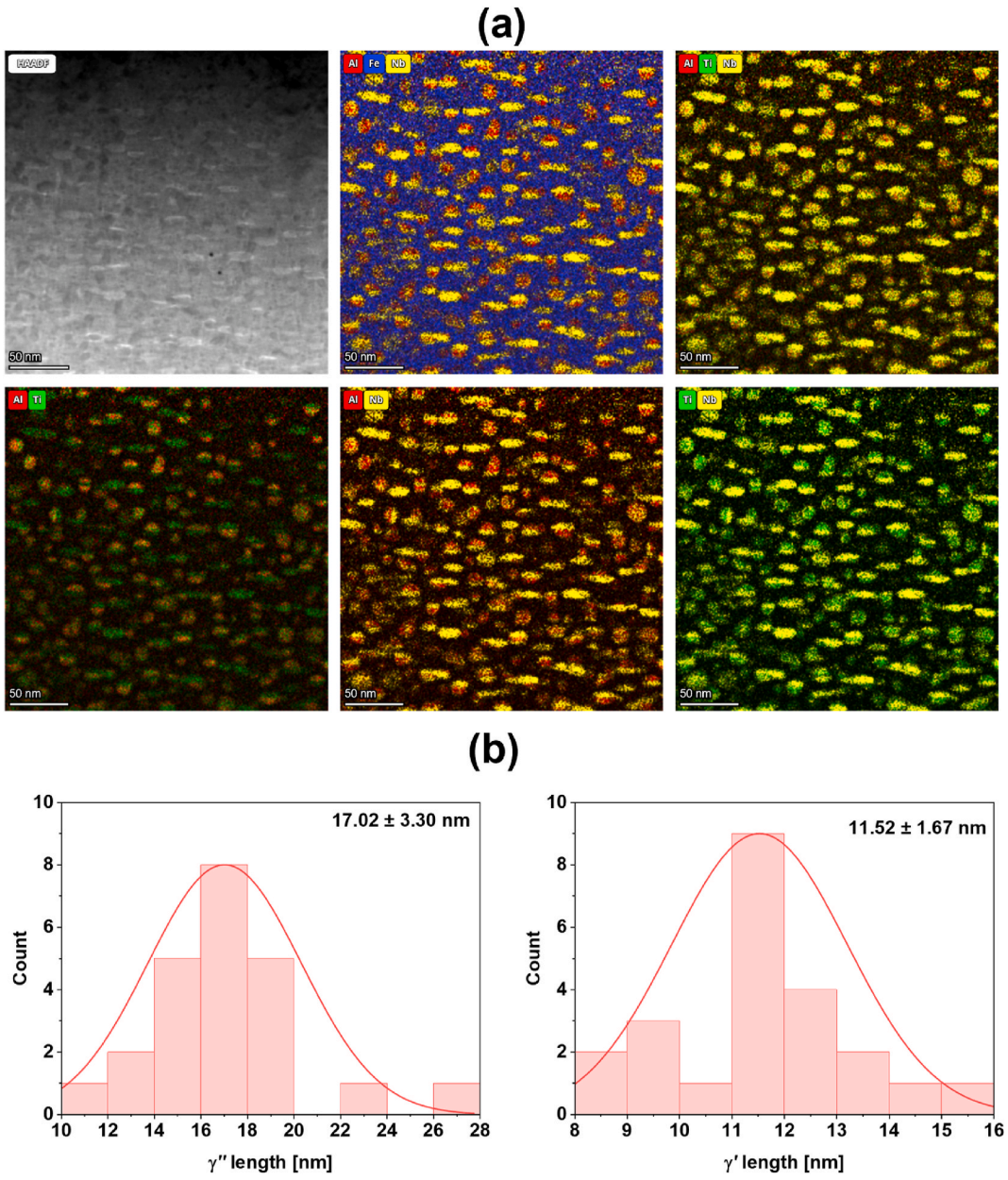

Fig. 6. – (a) Transmission electron microscopy coupled with energy dispersive X-Ray spectroscopy analysis of Inconel 718 fabricated by arc-based directed energy deposition (heat-treated) and (b) γ'' and γ' particle analysis (refer to Supplementary Material).

meeting the *UTS* requirement of AMS 5662 becomes a significant challenge for IN718 arc-based DED due to its non-optimized microstructure (coarse and oriented), which induces lower strain-hardening during the tensile test. This is reflected in the available literature (Table 4), which reports that only Xi et al. [17,18,90] (IN718 arc-based DED using cold metal transfer – CMT – process) met the AMS 5662 requirements through the conventional process route (3D printing + heat treatment). Xi et al. [17,18,90] attributed this achievement to the finer grain size induced by CMT-DED in relation to the regular GMA-based DED (i.e., lower heat input) [17,18] and the δ phase precipitation promoted by an intermediate solution heat treatment (900 °C/1 h) [90]. These two factors tend to increase the strain-hardening during the tensile test. In the present work, the δ phase was not observed because the adopted heat treatment did not include a solution step [23]. Additionally, a regular GMA welding machine was used (see Section 2.1), which tends to induce a coarse grain size compared to plasma transferred arc and/or GMA-CMT [12,99].

Despite the coarse and oriented microstructure (Fig. 5), the IN718 arc-based DED did not exhibit a remarkable *YS* anisotropy (9.8 %), as calculated following Kok et al. [100]. According to Hosford [71], the *YS* anisotropy can be estimated using the typical power-law hardening correlation between the shear strain (γ) and stress ($\tau = K\gamma^n$), as well as the Taylor factor definition $\left(M = \sum \frac{d\gamma}{d\varepsilon}\right)$. In addition, considering the relationship ($\sigma = M\tau$) between the applied stress (σ) and shear stress (τ) in a uniaxial tensile test, σ can be related to M (Equation (1)). Thus, the anisotropic index (A_i, Equation (2)) can be correlated with the tensile test curve profile (namely n) and microstructure/texture aspects (namely M) through Equation (3). σ_H, σ_V, and K, in Equations (1)–(3), represent the *YS* for the horizontal and vertical directions and the proportionality constant, respectively. The calculated (9.4 %, Equation (3)) and experimentally measured (9.8 %, Equation (2)) anisotropic indexes showed good agreement. This indicates that, despite the coarse and oriented microstructure of IN718 arc-based DED, which is expected to

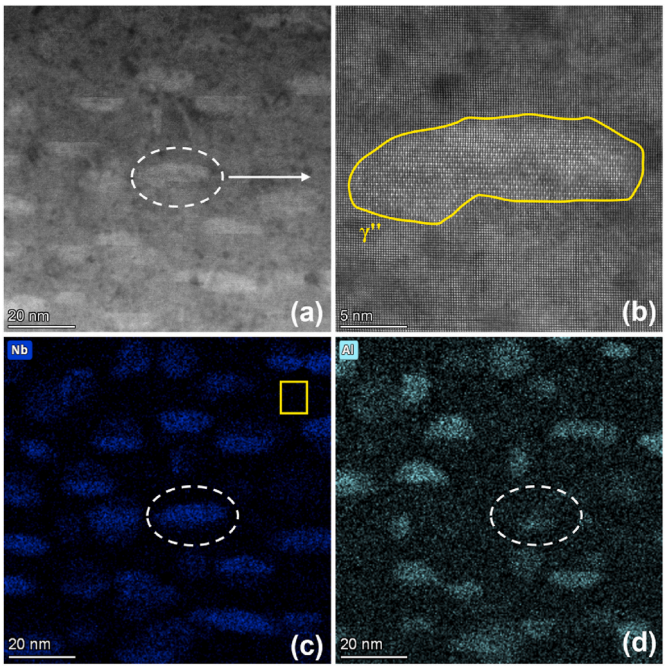

Fig. 7. – (a) and (b) High-magnification transmission electron microscopy images illustrating the precipitation of γ″ monoliths. (c) and (d) Energy dispersive X-Ray spectroscopy images highlighting the Al enrichment on one side of the γ″ monoliths. These analyses were performed on Inconel 718 fabricated by arc-based directed energy deposition (heat-treated condition). The yellow rectangle in (c) indicates the region where the chemical composition of the γ matrix was measured. (For interpretation of the references to colour in this figure legend, the reader is referred to the Web version of this article.)

Table 3
– γ′ and γ″ quantification through Rietveld refinement (Fig. 3) and quantitative metallography (Fig. 6).

	Rietveld refinement	Quantitative metallography
γ′ (Ni_3(Al, Ti); cubic; $L1_2$; Pm $\bar{3}$ m)	4.15 ± 0.41	5.01
γ″ (Ni_3Nb; $D0_{22}$; tetragonal; I4/mmm)	17.39 ± 1.74	17.02

promote significant mechanical anisotropy, the significant cube texture in both directions and the lower strain-hardening exponent mitigated the anticipated strong anisotropy. This enables the IN718 arc-based DED to achieve a A_i comparable to that of laser-based PBF, despite the more pronounced texture and coarser microstructure of arc-based DED [100–103].

$$\sigma = M^{n+1} K \varepsilon^n \tag{1}$$

$$A_i = \frac{|\sigma_H - \sigma_V|}{\sigma_V} \tag{2}$$

$$A_i = \frac{\left|M_H^{n_H+1} K \varepsilon^{n_H} - M_V^{n_V+1} K \varepsilon^{n_V}\right|}{M_V^{n_V+1} K \varepsilon^{n_V}} \tag{3}$$

$$A_i = \frac{\left|M_H^{n+1} - M_V^{n+1}\right|}{M_V^{n+1}}, n_V \approx n_H$$

3.3. Strengthening mechanisms

This section is dedicated to elucidating the remarkable yield strength of the IN718 arc-based DED (Table 4) through a (semi)quantitative experimentally-based strengthening mechanism analysis.

3.3.1. Peierls-Nabarro stress

The Peierls-Nabarro stress (σ_0) is expressed by Equation (4). M and τ_{crss} are the Taylor factor (Fig. 5) and the critical resolved shear stress (17.5 MPa [104]), respectively. The Peierls-Nabarro stress was calculated for horizontal (43.23 MPa) and vertical (47.25 MPa) directions.

$$\sigma_0 = M \tau_{crss} \tag{4}$$

3.3.2. Grain boundary

The grain boundary strengthening (σ_{gb}) was described using the Hall-Petch relation (Equation (5)) [82,105]. d and α represent the grain size (intercept method, ASTM E112) and the constant of proportionality (710 MPa $\mu m^{-0.5}$) [105,106]. The grain size was measured for both vertical and horizontal directions (1388.2 ± 588.8 and 373.6 ± 96.8, respectively; see Supplementary Material). σ_{gb} for vertical and horizontal directions was estimated to be 19.41 and 36.76 MPa, respectively. Thus, the observed difference in *YS* for both directions (~113 MPa) cannot be entirely explained through the grain size and its morphology (stereology). In addition, due to the coarse grain size (Fig. 5), grain boundary strengthening was classified as secondary for IN718 arc-based DED.

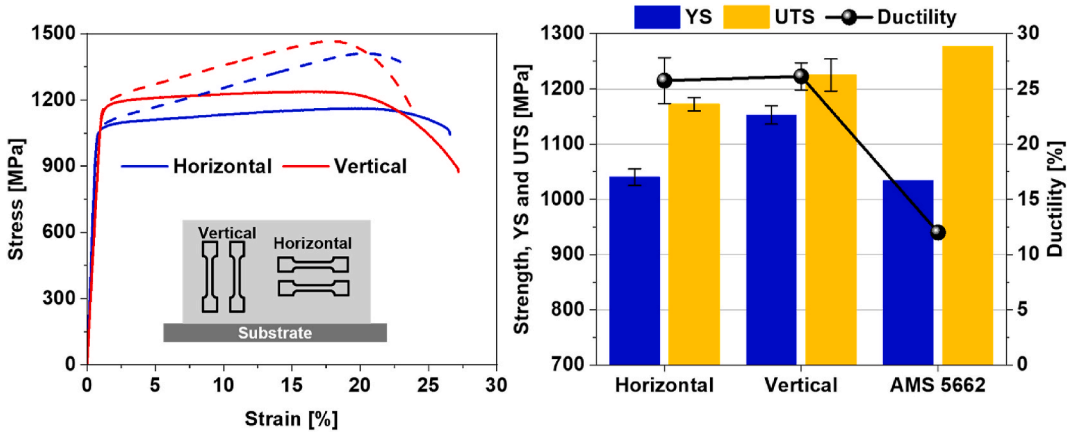

Fig. 8. – Tensile test of Inconel 718 fabricated by arc-based directed energy deposition (heat-treated condition). The dashed and solid lines represent the true and engineering stress-strain curves, respectively. The vertical and horizontal directions correspond to specimens aligned parallel and transverse to the building direction (Fig. 5). AMS 5662 is a standard that regalement the use of Inconel 718 in the aviation industry.

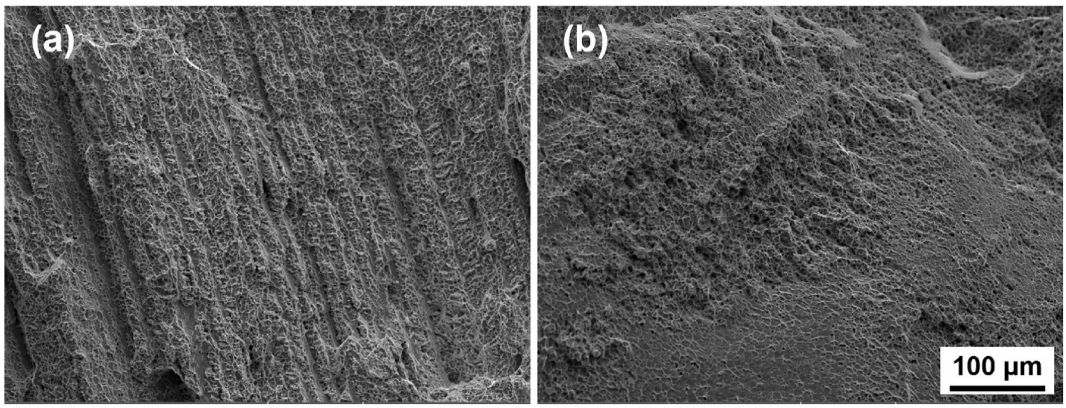

Fig. 9. – Fractography of tensile tests: (a) horizontal and (b) vertical.

Table 4
– Uniaxial tensile test of the IN718 fabricated by arc-based DED.

Reference	Heat treatment	Orientation	*YS* [MPa]	*UTS* [MPa]	Ductility [%]
Present work	1100 °C/2 h + aging	Horizontal	1040 ± 15	1172 ± 12	25.1 ± 2
		Vertical	1153 ± 17	1225 ± 29	26.1 ± 1.2
Xu et al. [25]	AMS 5662	Horizontal	790 ± 9	1102 ± 78	14.7 ± 1.3
		Vertical	791 ± 14	988 ± 6	12.8 ± 1.2
Kindermann et al. [16]	AMS 5662	Horizontal	910 ± 2	1185 ± 80	8.8 ± 3.4
		Vertical	1025 ± 9	1246 ± 117	6.2 ± 4.5
	API 6ACRA	Horizontal	780 ± 6	1304 ± 41	22.8 ± 3.2
		Vertical	842 ± 4	1229 ± 136	12.7 ± 5
Xu et al. [11]	AMS 5662	Horizontal	807 ± 1	1110 ± 3	15 ± 0.3
		Vertical	899 ± 5	1233 ± 16	19.4 ± 2.8
Xi et al. [17]	1185 °C/1 h + aging	Horizontal	1070 ± 9	1249 ± 30	20.09 ± 3
		Vertical	1071 ± 11	1251 ± 27	21.43 ± 3.9
Xi et al. [18]	1150 °C/1 h + aging		1070 ± 8.3	1270 ± 1	30.27 ± 1.38
Xi et al. [90]	1150 °C/1 h + 900 °C/1 h + aging		1071 ± 19	1316 ± 34	18.98 ± 3.97
Zhang et al. [19–22]	AMS 5662		865 ± 32	947 ± 43	7.16 ± 0.05
Chen et al. [91]	AMS 5383		1019	1111	9.8
Seow et al. [12]	AMS 5383	Horizontal	1065	1116	0.9
		Vertical	951	1072	2
	1185 °C/40 min + aging		856	1044	19.9
Wang et al. [92]	AMS 5662		864 ± 24	1152 ± 28	23 ± 2
James et al. [93]	AMS 5662		852	870	
AMS 5662			1034	1276	12
AMS 5383			724	827	3
API 6ACRA			965	1103	20
ASTM F3055			940	1240	12

$$\sigma_{gb} = \frac{\alpha}{d^{0.5}} \tag{5}$$

3.3.3. Dislocation density

The SXRD peaks for IN718 arc-based DED (heat-tread condition, Fig. 3) were fitted using a gaussian function (Supplementary Material) and the main peak characteristics were estimated (e.g., the Bragg's angle, θ, and full width at half maximum, FWHM). Using the Williamson and Hall [107] and Smallman and Westmacott [108] relations (Fig. 10), the statistically stored dislocations density (ρ, $3.33{\cdot}10^{13}$ m^{-2}) [109] was estimated from θ and FWHM [110,111]. The dislocatin density strengthening (σ_d) was computed using the Bailey-Hirsh's relation (Equation (6) [112]. b and G (65.9 GPa [113]) are the Burgers vector and shear modulus, respectively. b (0.2539 nm) was computed from SXRD peak fitting (Supplementary Material), using a procedure similar to those adopted by Farias et al. [30]. σ_d for the horizontal and vertical directions were 47.7 and 52.14 MPa, respectively. As the grain boundary strengthening mechanism, the dislocation density strengthening had a minimal influence on *YS* and only slightly contributed to *YS* anisotropy. The lower contribution of σ_d to *YS* can be associated to the lower intragranular residual strain caused by the relatively slower cooling rate of arc-based DED compared to high-density AM processes (e.g., PBF) [44,114,115]. Additionally, the long soaking time (2 h) and high peak temperature (1100 °C) of the heat treatment can promote recovery and dislocation annihilation [116].

$$\sigma_d = 0.2MbG\rho^{0.5} \tag{6}$$

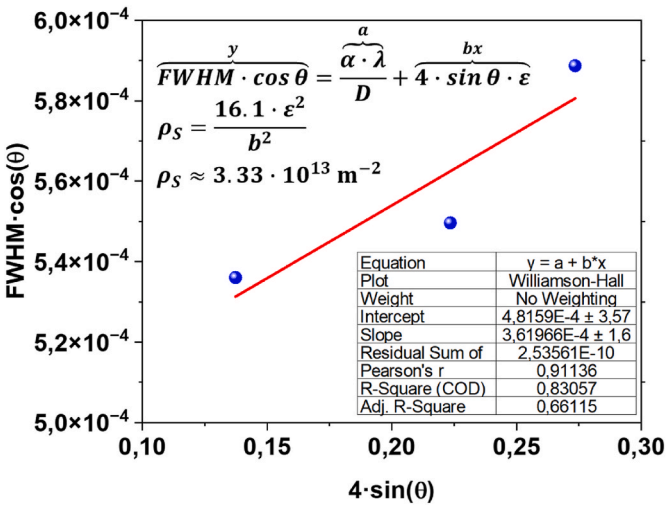

Fig. 10. – Williamson-Hall plot and dislocation density calculation.

Table 5
– Chemical composition in solid solution and the solid-solution strengthening (σ_{ss}) effect.

Composition, c_i [at.%]		Strengthening constants, a_i [MPa·at.%$^{-0.5}$] [122]	σ_{ss} [MPa]
Cr	21.89	337	245.62
Fe	25.35	153	
Al	0.79	225	
Nb	0.76	1183	
Ti	0.33	775	
Mo	1.6	1015	

3.3.4. Solid-solution

The chemical composition (c_i) of the γ matrix (Table 5), i.e., a region without precipitates, was measured using TEM-EDS (yellow rectangular box in Fig. 7). Solid-solution strengthening (σ_{ss}) was calculated using the Gypen and Deruyttere relation [117] (Equation (7) and Table 5). The strengthening constants (a_i) for each alloying element are detailed in Table 5. The obtained result (~246 MPa) was close to that found by Zhang et al. [44] (250 MPa, IN718 PBF) and inferior to Sui et al. [39] (181 MPa, IN718 laser-based DED), highlighting the effect of heat treatment and cooling rate (AM process) on the solid-solution strengthening. The higher σ_{ss} effect for IN718 arc-based DED compared to laser-based DED can be attributed to its slower cooling rate (i.e., higher interdendritic segregation) [50,118–121] and the partial dissolution of Laves phase (Fig. 1), which induces a higher alloying element content in solid solution, particularly in the vicinity of the interdendritic regions. As described by Gypen and Deruyttere relation, σ_{ss} is isotropic and cannot be associated with the observed anisotropy. Furthermore, σ_{ss} corresponds to 20–24 % of the *YS*, being classified as the second most important strengthening mechanism for IN718 arc-based DED.

$$\sigma_{ss} = \left[\sum_i \left(a_i c_i^{0.5}\right)^2\right]^{0.5} \tag{7}$$

3.3.5. Precipitation

As previously indicated by SEM, SXRD, and TEM analyses, the IN718 arc-based DED presents several secondary phases (MC-type carbide, Laves, γ″, and γ′), which can interact with the dislocations in motion and contribute to material strengthening [72]. Orowan's bypass mechanism, typically associated with incoherent second phases (MC-type carbides and Laves phases), is characterized by dislocation bowing and climbing [35,123], i.e., a thermally activated phenomenon. Thus, dislocation bowing in coarse and incoherent secondary phases of Ni-based superalloys at room temperature is not typically observed [124,125]. Moreover, according to Kelly's model [126], the coarse particle sizes of MC-type carbides and Laves (micrometric-sized vs. nanometric-sized γ″ and γ′) will result in negligible strengthening through the dispersion of secondary phases. Furthermore, Farias et al. [26] and Sui et al. [39], IN718 fabricated by arc- and laser-based DED, respectively, reported that the low volume fraction of Laves phase and MC-type carbides (eutectics) aligns with their coarse particle size, promoting an insignificant effect on the final material strengthening. Thus, the present work did not compute the interdendritic eutectics effect on IN718 arc-based DED strength.

Zhang et al. [44] and Farabi et al. [127] reported that, for γ″ and γ′ particle size expressed in Fig. 6, the coherency (γ″) and order (γ′) mechanisms govern the precipitate strengthening mechanism. Additionally, Chaturvedi and Han [36] pointed out that the γ′ order strengthening ($\sigma_{\gamma'}$; Equation (8)) and γ″ coherency strengthening ($\sigma_{\gamma''}$; Equation (9)) [106,128,129] mechanisms exhibited the best approximation between the computed and experimentally estimated resolved shear stress. Therefore, $\sigma_{\gamma'}$ and $\sigma_{\gamma''}$ were adopted in the present work to estimate the IN718 arc-based DED strength (heat-treated condition). All the variable names and input data used in Equations (8) and (9) were presented in Table 6. $\sigma_{\gamma'}$ (81.17 and 88.73 MPa) and $\sigma_{\gamma''}$ (649.61 and 710.1 MPa) were computed in horizontal and vertical directions, respectively, which confirms that the γ″ coherency strengthening was the primary strengthening mechanism for IN718 arc-based DED. Similar results have previously been observed for fusion-based AM processes and casting [26,32,39,44]. Furthermore, γ″ coherency strengthening was primarily associated with the *YS* anisotropy, reinforcing the *YS* anisotropy dependence on γ″ volume fraction, γ″ particle size, and matrix crystallographic texture (i.e., Taylor factor), as indicated by Equation (9).

Table 6
– Physical constants used in Equations (8) and (9).

Taylor factor, M	2.7 and 2.47, Fig. 5
Phase content, f	5.01 and 17.02, Table 3
Burgers vector, b	0.2539 nm, Supplementary Material
Shear modulus, G	65.9 GPa [113]
Antiphase boundary energy, γ'_{APB}	12 mJ/m^2 [128]
Average length of γ′ phase, $2R_{\gamma'}$	11.52 nm, Fig. 6
Average length of γ″ phase, $2R_{\gamma''}$	17.02 nm, Fig. 6
Average thickness of γ″ phase, e	6.51 nm, Supplementary Material
γ″ lattice misfit, $\delta_{\gamma''}$	0.02364, Supplementary Material

$$\sigma_{\gamma'} = M\frac{\gamma'_{APB}}{2b}\left[\left(\frac{8\gamma'_{APB}fR_{\gamma'}}{\pi Gb^2}\right)^{0.5} - f\right] \tag{8}$$

$$\sigma_{\gamma''} = 1.7GM\delta_{\gamma''}^{1.5}\left[\frac{R_{\gamma''}f}{2b\left(\frac{2R_{\gamma''}}{e}\right)^2}\right]^{0.5} \tag{9}$$

3.3.6. Combined effect

The combined contributions (σ_y) of the aforementioned strengthening mechanisms were computed as expressed in Equation (10) [106,130]. Table 7 and Fig. 11 summarize the contributions of the strengthening mechanisms and compare the (semi)quantitative analysis with the experimentally measured *YS*, showing good agreement (relative error less than 5 %) and validating the experimentally-based strengthening mechanism analysis previously presented (Sections 3.3.1–3.3.5).

$$\sigma_y = \sigma_0 + \sigma_{gb} + \sigma_d + \sigma_{ss} + \sigma_{\gamma'} + \sigma_{\gamma''} \tag{10}$$

Table 7
– Combined effects of the strengthening mechanisms in Inconel 718 fabricated by arc-based directed energy deposition (heat-treated condition).

Strengthening mechanism		Horizontal	Vertical
Peierls-Nabarro stress, σ_0	$M\tau_{crss}$	43.23	47.25
Grain boundary, σ_{gb}	$\frac{\alpha}{d^{0.5}}$	19.41	36.76
Dislocation density, σ_d	$0.2MbG\rho^{0.5}$	47.70	52.14
Solid solution, σ_{ss}	$\left[\sum_i \left(a_i c_i^{0.5}\right)^2\right]^{0.5}$	245.62	245.62
γ′ order, $\sigma_{\gamma'}$	$M\frac{\gamma'_{APB}}{2b}\left[\left(\frac{8\gamma'_{APB}fR_{\gamma'}}{\pi Gb^2}\right)^{0.5} - f\right]$	81.17	88.73
γ″ coherency, $\sigma_{\gamma''}$	$1.7GM\delta_{\gamma''}^{1.5}\left[\frac{R_{\gamma''}f}{2b\left(\frac{2R_{\gamma''}}{e}\right)^2}\right]^{0.5}$	649.61	710.10
Estimated yield strength, σ_y	$\sigma_0 + \sigma_{gb} + \sigma_d + \sigma_{ss} + \sigma_{\gamma'} + \sigma_{\gamma''}$	1086.73	1180.60
Measured yield strength[a]		1040 ± 15	1153 ± 17
Relative error [%]		4.49	2.39

[a] Tensile test, Fig. 8 and Table 4.

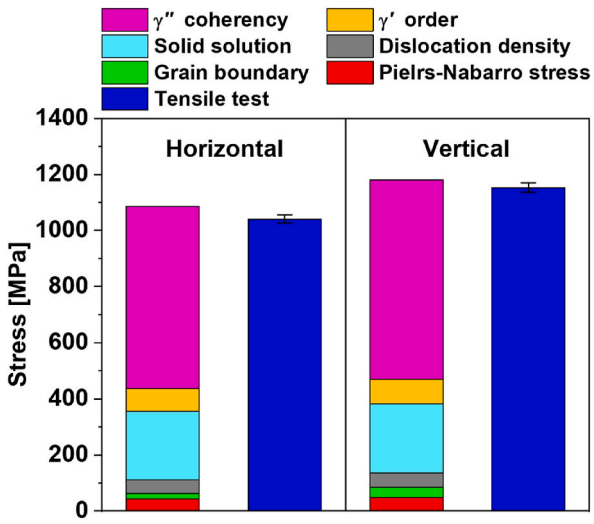

Fig. 11. – Comparison between the physically-based quantitative strengthening mechanism analysis and the experimentally measured yield strength for vertical and horizontal directions.

The observed yield strength anisotropy can be directly correlated with the effect of Taylor factor (i.e., crystallographic texture aspects) on strengthening mechanisms, which has a linear effect on Peierls-Nabarro stress (Equation (4), dislocation density (Equation (6)), and precipitation (Equations (8) and (9)) strengthening mechanisms. In addition, grain morphology and stereology also contributed to anisotropy (17.35 MPa); however, at an inferior level in relation to the Taylor factor (76.51 MPa). From Fig. 11, it is evident that the precipitation strengthening mechanism governs the final strength of the IN718 arc-based DED, especially the γ″ coherency strengthening. This reveals operational implications during process optimization and heat treatment development, which must focus on increasing the Nb (γ″-former) content available in solid solution. As a consequence, it is possible to achieve an appreciable γ″ volume fraction, ensuring that strict strength requirements (e.g., AMS 5662) can be met (Table 4), even with a non-optimized microstructure (coarse and oriented). Moreover, as indicated by Equations ((4), (6), (8) and (9), increasing the average Taylor factor, i.e., altering the cryptographic texture aspects, will also significantly alter the IN718 arc-based DED strength [18]. However, optimizing process parameters to alter the crystallographic texture is challenging because Inconel 718 has a narrow process window (i.e., preventing hot cracks and lack of fusion) [15,99,131]. This suggests the use of grain size refinement techniques, e.g., interlayer mechanical deformation [29], inoculants [132], and vibration [31], can be a suitable alternative for improving the primary microstructure of the IN718 arc-based DED.

4. Conclusions

The present work evaluated the microstructure and tensile properties of the Inconel 718 fabricated by arc-based DED (IN718 arc-based DED). In addition, the strengthening mechanism was described and quantitatively assessed through an experimentally-based procedure, showing a good agreement (error inferior to 5 %) with the measured yield strength. IN718 arc-based DED (as-built) exhibited a coarse and oriented microstructure with the presence of interdendritic eutectics (Laves and MC-type carbides). At heat-treated condition (1100 °C/2 h + aging), the Laves phase was partially dissolved; however, the grain stereology and crystallographic texture were unchanged. Additionally, despite the IN718 arc-based DED non-optimized microstructure, the heat treatment induced a significant content of γ″ and γ′ (~17 and 5 %), which results in a yield strength superior to that required by AMS 5662. The contribution of each strengthening mechanism was computed based on experimental data collected through EBSD, SXRD, and TEM, which evidenced that the precipitation strengthening mechanism governs the final strength of the IN718 arc-based DED. Furthermore, the analysis of strengthening mechanisms revealed that yield strength anisotropy was primarily associated with the linear dependence of these mechanisms – particularly precipitation hardening – on the Taylor factor (i.e., crystallographic texture), while grain size and morphology (stereology) played a secondary role in yield strength anisotropy.

CRediT authorship contribution statement

Francisco Werley Cipriano Farias: Writing – original draft, Methodology, Investigation, Formal analysis, Data curation, Conceptualization. **Valdemar Rebelo Duarte:** Writing – review & editing, Methodology, Formal analysis, Data curation, Conceptualization. **João da Cruz Payão Filho:** Supervision, Software, Resources, Methodology, Formal analysis. **Arthur Ribeiro Figueiredo:** Software, Formal analysis, Data curation, Conceptualization. **Norbert Schell:** Resources, Methodology. **Emad Maawad:** Resources, Investigation. **Fabio Machado Alves da Fonseca:** Resources, Methodology, Investigation, Data curation. **Jonathan Cormier:** Writing – review & editing, Resources, Methodology, Investigation, Funding acquisition, Formal analysis, Conceptualization. **Antonio J. Ramirez:** Supervision, Resources, Project administration, Methodology, Investigation, Funding acquisition. **Telmo G. Santos:** Writing – review & editing, Supervision, Resources, Project administration, Methodology, Investigation, Funding acquisition, Formal analysis, Data curation, Conceptualization. **J.P. Oliveira:** Writing – review & editing, Supervision, Resources, Project administration, Methodology, Investigation, Funding acquisition, Formal analysis, Data curation, Conceptualization.

Declaration of competing interest

The authors declare that they have no known competing financial interests or personal relationships that could have appeared to influence the work reported in this paper.

Acknowledgments

Authors acknowledge the Portuguese Fundação para a Ciência e a Tecnologia (FCT – MCTES) for its financial support via the project UID/EMS/00667/2019 (UNIDEMI). JPO acknowledges funding by national funds from FCT - Fundação para a Ciência e a Tecnologia, I.P., in the scope of the projects LA/P/0037/2020, UIDP/50025/2020 and UIDB/50025/2020 of the Associate Laboratory Institute of Nanostructures, Nanomodelling and Nanofabrication – i3N. Funding of CENIMAT/i3N by national funds through the FCT-Fundação para a Ciência e a Tecnologia, I.P., within the scope of Multiannual Financing of R&D Units, reference UIDB/50025/2020–2023 is also acknowledge. FWCF acknowledges Fundação para a Ciência e a Tecnologia (FCT-MCTES) for funding the Ph.D. Grant 2022.13870.BD. The authors acknowledge DESY (Hamburg, Germany), a member of the Helmholtz Association HGF, for the provision of experimental facilities. Beamtime was allocated for proposal I-20210986 EC. The research leading to this result has been supported by the project CALIPSOplus under the Grant Agreement 730872 from the EU Framework Programme for Research and Innovation HORIZON 2020. This activity has received funding from the European Institute of Innovation and Technology (EIT) Raw Materials through the project Smart WAAM: Microstructural Engineering and Integrated Non-Destructive Testing. FWCF acknowledges The Manufacturing and Materials Joining Innovation Center (MA^2JIC) and the Center for Electron Microscopy and Analysis (CEMAS) for available facilities used during the development of this work. Institut Pprime gratefully acknowledges “Contrat de Plan Etat - Région Nouvelle-Aquitaine (CPER)” as well as the “Fonds Européen de Développement

Régional (FEDER)" for their financial support to part of the reported work.

Appendix A. Supplementary data

Supplementary data to this article can be found online at https://doi.org/10.1016/j.msea.2025.148417.

Data availability

Data will be made available on request.

References

[1] R. Krakow, D.N. Johnstone, A.S. Eggeman, D. Hünert, M.C. Hardy, C.M.F. Rae, P. A. Midgley, On the crystallography and composition of topologically close-packed phases in ATI 718Plus®, Acta Mater. 130 (2017) 271–280, https://doi.org/10.1016/J.ACTAMAT.2017.03.038.

[2] N.C. Ferreri, S.C. Vogel, M. Knezevic, Determining volume fractions of γ, γ′, γ″, δ, and MC-carbide phases in Inconel 718 as a function of its processing history using an advanced neutron diffraction procedure, Mater. Sci. Eng. A 781 (2020) 139228, https://doi.org/10.1016/J.MSEA.2020.139228.

[3] A. Chamanfar, L. Sarrat, M. Jahazi, M. Asadi, A. Weck, A.K.K. Koul, Microstructural characteristics of forged and heat treated Inconel-718 disks, Mater. Des. 52 (2013) 791–800, https://doi.org/10.1016/j.matdes.2013.06.004.

[4] M. Rafiei, H. Mirzadeh, M. Malekan, Precipitation kinetics of γ″ phase and its mechanism in a Nb-bearing nickel-based superalloy during aging, Vacuum 178 (2020) 109456, https://doi.org/10.1016/J.VACUUM.2020.109456.

[5] A. Argon, Strengthening Mechanisms in Crystal Plasticity, Oxford University Press, 2007, https://doi.org/10.1093/acprof:oso/9780198516002.001.0001.

[6] N. Kwabena Adomako, N. Haghdadi, S. Primig, Electron and laser-based additive manufacturing of Ni-based superalloys: a review of heterogeneities in microstructure and mechanical properties, Mater. Des. 223 (2022) 111245, https://doi.org/10.1016/j.matdes.2022.111245.

[7] N. El-Bagoury, T. Matsuba, K. Yamamoto, H. Miyahara, K. Ogi, Influence of heat treatment on the distribution of Ni2Nb and microsegregation in cast inconel 718 alloy, Mater. Trans. 46 (2005) 2478–2483, https://doi.org/10.2320/MATERTRANS.46.2478.

[8] X. You, Y. Tan, S. Shi, J.-M.M. Yang, Y. Wang, J. Li, Q. You, Effect of solution heat treatment on the precipitation behavior and strengthening mechanisms of electron beam smelted Inconel 718 superalloy, Mater. Sci. Eng. A 689 (2017) 257–268, https://doi.org/10.1016/j.msea.2017.01.093.

[9] X. Liu, R. Hu, C. Yang, X. Luo, Y. Hou, J. Bai, R. Ma, Strengthening mechanism of a Ni-based superalloy prepared by laser powder bed fusion: the role of cellular structure, Mater. Des. 235 (2023) 112396, https://doi.org/10.1016/j.matdes.2023.112396.

[10] V.V. Rielli, F. Godor, C. Gruber, A. Stanojevic, B. Oberwinkler, S. Primig, Effects of processing heterogeneities on the micro- to nanostructure strengthening mechanisms of an alloy 718 turbine disk, Mater. Des. 212 (2021) 110295, https://doi.org/10.1016/j.matdes.2021.110295.

[11] X. Xu, J. Ding, S. Ganguly, S. Williams, Investigation of process factors affecting mechanical properties of INCONEL 718 superalloy in wire + arc additive manufacture process, J. Mater. Process. Technol. 265 (2019) 201–209, https://doi.org/10.1016/j.jmatprotec.2018.10.023.

[12] C.E. Seow, H.E. Coules, G. Wu, R.H.U. Khan, X. Xu, S. Williams, Wire + Arc Additively manufactured Inconel 718: effect of post-deposition heat treatments on microstructure and tensile properties, Mater. Des. 183 (2019) 108157, https://doi.org/10.1016/j.matdes.2019.108157.

[13] T. Bhujangrao, F. Veiga, A. Suárez, E. Iriondo, F.G. Mata, High-temperature mechanical properties of IN718 alloy: Comparison of additive manufactured and wrought samples, Crystals 10 (2020) 1–13, https://doi.org/10.3390/cryst10080689.

[14] U. Alonso, F. Veiga, A. Suárez, A. Gil Del Val, Characterization of Inconel 718® superalloy fabricated by wire Arc Additive manufacturing: effect on mechanical properties and machinability, J. Mater. Res. Technol. 14 (2021) 2665–2676, https://doi.org/10.1016/j.jmrt.2021.07.132.

[15] R.M. Kindermann, M.J. Roy, R. Morana, P.B. Prangnell, Process response of Inconel 718 to wire + arc additive manufacturing with cold metal transfer, Mater. Des. 195 (2020) 109031, https://doi.org/10.1016/j.matdes.2020.109031.

[16] R.M.M. Kindermann, M.J.J. Roy, R. Morana, J.A.A. Francis, Effects of microstructural heterogeneity and structural defects on the mechanical behaviour of wire + arc additively manufactured Inconel 718 components, Mater. Sci. Eng. A 839 (2022) 142826, https://doi.org/10.1016/j.msea.2022.142826.

[17] N. Xi, X. Fang, Y. Duan, Q. Zhang, K. Huang, Wire arc additive manufacturing of Inconel 718: constitutive modelling and its microstructure basis, J. Manuf. Process. 75 (2022) 1134–1143, https://doi.org/10.1016/j.jmapro.2022.01.067.

[18] N. Xi, K. Tang, X. Fang, Y. Li, Y. Duan, K. Huang, Enhanced comprehensive properties of directed energy deposited Inconel 718 by a novel integrated deposition strategy, J. Mater. Sci. Technol. 141 (2023) 42–55, https://doi.org/10.1016/j.jmst.2022.09.026.

[19] T. Zhang, H. Li, H. Gong, Y. Wu, A.S. Ahmad, X. Chen, Effect of rolling force on tensile properties of additively manufactured Inconel 718 at ambient and elevated temperatures, J. Alloys Compd. 884 (2021) 161050, https://doi.org/10.1016/j.jallcom.2021.161050.

[20] T. Zhang, H. Li, H. Gong, J. Ding, Y. Wu, C. Diao, X. Zhang, S. Williams, Hybrid wire - arc additive manufacture and effect of rolling process on microstructure and tensile properties of Inconel 718, J. Mater. Process. Technol. 299 (2022) 117361, https://doi.org/10.1016/j.jmatprotec.2021.117361.

[21] T. Zhang, H. Li, H. Gong, Y. Wu, A.S. Ahmad, X. Chen, X. Zhang, Comparative analysis of cold and warm rolling on tensile properties and microstructure of additive manufactured Inconel 718, Arch. Civ. Mech. Eng. 22 (2022) 1–14, https://doi.org/10.1007/s43452-021-00356-7.

[22] T. Zhang, H. Li, H. Gong, Y. Wu, X. Chen, X. Zhang, Study on location-related thermal cycles and microstructure variation of additively manufactured Inconel 718, J. Mater. Res. Technol. 18 (2022) 3056–3072, https://doi.org/10.1016/j.jmrt.2022.03.178.

[23] J. Jang, D. Van, S.H. Lee, Precipitation kinetics of secondary phases induced by heat accumulation in the deposit of Inconel 718, Addit. Manuf. (2022) 102831, https://doi.org/10.1016/J.ADDMA.2022.102831.

[24] J. Hönnige, C.E. Seow, S. Ganguly, X. Xu, S. Cabeza, H. Coules, S. Williams, Study of residual stress and microstructural evolution in as-deposited and inter-pass rolled wire plus arc additively manufactured Inconel 718 alloy after ageing treatment, Mater. Sci. Eng. A 801 (2021) 140368, https://doi.org/10.1016/j.msea.2020.140368.

[25] X. Xu, S. Ganguly, J. Ding, C.E. Seow, S. Williams, Enhancing mechanical properties of wire + arc additively manufactured INCONEL 718 superalloy through in-process thermomechanical processing, Mater. Des. 160 (2018) 1042–1051, https://doi.org/10.1016/j.matdes.2018.10.038.

[26] F.W.C. Farias, V.R. Duarte, J. da C.P. Filho, A.R. Figueiredo, N. Schell, E. Maawad, J.Y. Li, Y. Zhang, M. Bordas-Czaplicki, F.M.A. da Fonseca, J. Cormier, T.G. Santos, J.P. Oliveira, High-performance Ni-based superalloy 718 fabricated via arc plasma directed energy deposition: effect of post-deposition heat treatments on microstructure and mechanical properties, Addit. Manuf. 88 (2024) 104252, https://doi.org/10.1016/j.addma.2024.104252.

[27] W. Gao, J. Lu, J. Zhou, L. Liu, J. Wang, Y. Zhang, Z. Zhang, Effect of grain size on deformation and fracture of Inconel718: an in-situ SEM-EBSD-DIC investigation, Mater. Sci. Eng. A 861 (2022) 144361, https://doi.org/10.1016/j.msea.2022.144361.

[28] F. Theska, A. Stanojevic, B. Oberwinkler, S. Primig, Microstructure-property relationships in directly aged alloy 718 turbine disks, Mater. Sci. Eng. A 776 (2020) 138967, https://doi.org/10.1016/j.msea.2020.138967.

[29] F.W.C. Farias, T.J.G. dos Santos, J.P. Oliveira, Directed energy deposition + mechanical interlayer deformation additive manufacturing: a state-of-the-art literature review, Int. J. Adv. Manuf. Technol. 131 (2024) 999–1038, https://doi.org/10.1007/s00170-024-13126-5.

[30] F.W.C. Farias, V.R. Duarte, I.O. Felice, J. da C.P. Filho, N. Schell, E. Maawad, J. Y. Li, Y. Zhang, T.G. Santos, J.P. Oliveira, In situ interlayer hot forging arc plasma directed energy deposition of inconel® 625: microstructure evolution during heat treatments, J. Alloys Compd. 952 (2023) 170059, https://doi.org/10.1016/j.jallcom.2023.170059.

[31] Y. Chen, M. Xu, T. Zhang, J. Xie, K. Wei, S. Wang, L. Yin, P. He, Grain refinement and mechanical properties improvement of Inconel 625 alloy fabricated by ultrasonic-assisted wire and arc additive manufacturing, J. Alloys Compd. 910 (2022) 164957, https://doi.org/10.1016/j.jallcom.2022.164957.

[32] L.S.B. Ling, Z. Yin, Z. Hu, J.H. Liang, Z.Y. Wang, J. Wang, B. De Sun, Effects of the γ″-Ni3Nb phase on mechanical properties of inconel 718 superalloys with different heat treatments, Materials (Basel) 13 (2019) 151, https://doi.org/10.3390/MA13010151.

[33] F. Theska, A. Stanojevic, B. Oberwinkler, S.P. Ringer, S. Primig, On conventional versus direct ageing of Alloy 718, Acta Mater. 156 (2018) 116–124, https://doi.org/10.1016/j.actamat.2018.06.034.

[34] A. Ribeiro Figueiredo, L.M.B. de Azevedo, F. da Cruz Gallo, M.A. Ramalho Medeiros, L.H. de Almeida, L.S. Araújo, A. da Cunha Rocha, Effect of annealing twins, strain-recrystallization processing and δ-phase fraction on microtexture and evaluation of mechanical properties of nickel-based superalloy 718, Mater. Sci. Eng. A 881 (2023) 145341, https://doi.org/10.1016/j.msea.2023.145341.

[35] A.J. Goodfellow, Strengthening mechanisms in polycrystalline nickel-based superalloys, Mater. Sci. Technol. 34 (2018) 1793–1808, https://doi.org/10.1080/02670836.2018.1461594.

[36] M.C. Chaturvedi, Y.F. Han, Strengthening mechanisms in Inconel 718 superalloy, Met. Sci. 17 (1983) 145–149, https://doi.org/10.1179/030634583790421032.

[37] S. Tabaie, F. Rézaï-Aria, B.C.D. Flipo, M. Jahazi, Dissimilar linear friction welding of selective laser melted Inconel 718 to forged Ni-based superalloy AD730™: evolution of strengthening phases, J. Mater. Sci. Technol. 96 (2022) 248–261, https://doi.org/10.1016/j.jmst.2021.03.086.

[38] C. Joseph, C. Persson, M. Hörnqvist Colliander, Influence of heat treatment on the microstructure and tensile properties of Ni-base superalloy Haynes 282, Mater. Sci. Eng. A 679 (2017) 520–530, https://doi.org/10.1016/j.msea.2016.10.048.

[39] S. Sui, H. Tan, J. Chen, C. Zhong, Z. Li, W. Fan, A. Gasser, W. Huang, The influence of Laves phases on the room temperature tensile properties of Inconel 718 fabricated by powder feeding laser additive manufacturing, Acta Mater. 164 (2019) 413–427, https://doi.org/10.1016/J.ACTAMAT.2018.10.032.

[40] P. Sun, N. Yan, S. Wei, D. Wang, W. Song, C. Tang, J. Yang, Z. Xu, Q. Hu, X. Zeng, Microstructural evolution and strengthening mechanisms of Inconel 718 alloy with different W addition fabricated by laser cladding, Mater. Sci. Eng. A 868 (2023) 144535, https://doi.org/10.1016/j.msea.2022.144535.

[41] J. Liang, Z. He, W. Du, X. Ruan, E. Guo, N. Shen, Tailoring the microstructure and mechanical properties of laser metal-deposited Hastelloy X superalloy sheets via

post heat-treatment, Mater. Sci. Eng. A 884 (2023) 145546, https://doi.org/10.1016/j.msea.2023.145546.
[42] S. Birosca, F. Di Gioacchino, S. Stekovic, M. Hardy, A quantitative approach to study the effect of local texture and heterogeneous plastic strain on the deformation micromechanism in RR1000 nickel-based superalloy, Acta Mater. 74 (2014) 110–124, https://doi.org/10.1016/j.actamat.2014.04.039.
[43] O. Gokcekaya, T. Ishimoto, S. Hibino, J. Yasutomi, T. Narushima, T. Nakano, Unique crystallographic texture formation in Inconel 718 by laser powder bed fusion and its effect on mechanical anisotropy, Acta Mater. 212 (2021) 116876, https://doi.org/10.1016/j.actamat.2021.116876.
[44] S. Zhang, X. Lin, L. Wang, X. Yu, Y. Hu, H. Yang, L. Lei, W. Huang, Strengthening mechanisms in selective laser-melted Inconel718 superalloy, Mater. Sci. Eng. A 812 (2021) 141145, https://doi.org/10.1016/j.msea.2021.141145.
[45] V.R. Duarte, T.A. Rodrigues, N. Schell, R.M. Miranda, J.P. Oliveira, T.G. Santos, In-situ hot forging direct energy deposition-arc of CuAl8 alloy, Addit. Manuf. (2022) 102847, https://doi.org/10.1016/j.addma.2022.102847.
[46] R. Hielscher, H. Schaeben, A novel pole figure inversion method: specification of the MTEX algorithm, J. Appl. Crystallogr. 41 (2008) 1024–1037, https://doi.org/10.1107/S0021889808030112.
[47] A.P. Hammersley, S.O. Svensson, M. Hanfland, A.N. Fitch, D. Häusermann, Two-dimensional detector software: from real detector to idealised image or two-theta scan, High Press. Res. 14 (1996) 235–248, https://doi.org/10.1080/08957959608201408.
[48] T.A. Rodrigues, F.W.C. Farias, J.A. Avila, E. Maawad, N. Schell, T.G. Santos, J. P. Oliveira, Effect of heat treatments on Inconel 625 fabricated by wire and arc additive manufacturing: an in situ synchrotron X-ray diffraction analysis, Sci. Technol. Weld. Join. 28 (2023) 1–6, https://doi.org/10.1080/13621718.2023.2187927.
[49] L. Ling, Y. Han, W. Zhou, H. Gao, D. Shu, J. Wang, M. Kang, B. Sun, Study of microsegregation and laves phase in INCONEL718 superalloy regarding cooling rate during solidification, Metall. Mater. Trans. A. 46 (2015) 354–361, https://doi.org/10.1007/s11661-014-2614-5.
[50] F.W.C. Farias, J. da C. Payão Filho, V.H.P. Moraes e Oliveira, Prediction of the interpass temperature of a wire arc additive manufactured wall: FEM simulations and artificial neural network, Addit. Manuf. 48 (2021) 102387, https://doi.org/10.1016/j.addma.2021.102387.
[51] H. Qi, M. Azer, A. Ritter, Studies of standard heat treatment effects on microstructure and mechanical properties of laser net shape manufactured INCONEL 718, Metall. Mater. Trans. A. 40 (2009) 2410–2422, https://doi.org/10.1007/s11661-009-9949-3.
[52] J.N. DuPont, C.V. Robino, J.R. Michael, M.R. Nous, A.R. Marder, Solidification of Nb-bearing superalloys: part I. Reaction sequences, Metall. Mater. Trans. A. 29 (1998) 2785–2796, https://doi.org/10.1007/S11661-998-0319-3.
[53] S.A. Oh, R.E. Lim, J.W. Aroh, A.C. Chuang, B.J. Gould, J. V Bernier, N. Parab, T. Sun, R.M. Suter, A.D. Rollett, Microscale observation via high-speed X-ray diffraction of alloy 718 during in Situ laser melting, J. Occup. Med. 73 (2021) 212–222, https://doi.org/10.1007/s11837-020-04481-1.
[54] C.C. Silva, H.C. de Miranda, M.F. Motta, J.P. Farias, C.R.M. Afonso, A.J. Ramirez, New insight on the solidification path of an alloy 625 weld overlay, J. Mater. Res. Technol. 2 (2013) 228–237, https://doi.org/10.1016/j.jmrt.2013.02.008.
[55] M. Solecka, A. Kopia, A. Radziszewska, B. Rutkowski, Microstructure, microsegregation and nanohardness of CMT clad layers of Ni-base alloy on 16Mo3 steel, J. Alloys Compd. 751 (2018) 86–95, https://doi.org/10.1016/j.jallcom.2018.04.102.
[56] K. Kakehi, S. Banoth, Y.-L. Kuo, S. Hayashi, Effect of yttrium addition on creep properties of a Ni-base superalloy built up by selective laser melting, Scr. Mater. 183 (2020) 71–74, https://doi.org/10.1016/j.scriptamat.2020.03.014.
[57] Y.-L. Kuo, K. Kakehi, Influence of powder surface contamination in the Ni-Based superalloy Alloy718 fabricated by selective laser melting and hot isostatic pressing, Metals (Basel). 7 (2017) 367, https://doi.org/10.3390/met7090367.
[58] Y.N. Zhang, X. Cao, P. Wanjara, M. Medraj, Oxide films in laser additive manufactured Inconel 718, Acta Mater. 61 (2013) 6562–6576, https://doi.org/10.1016/j.actamat.2013.07.039.
[59] Q. Pang, G.H. Wu, Z.Y. Xiu, L.T. Jiang, D.L. Sun, Microstructure, oxidation resistance and high-temperature strength of a new class of 3D open-cell nickel-based foams, Mater. Charact. 70 (2012) 125–136, https://doi.org/10.1016/J.MATCHAR.2012.05.010.
[60] Q. Jia, D. Gu, Selective laser melting additive manufactured Inconel 718 superalloy parts: High-temperature oxidation property and its mechanisms, Opt Laser. Technol. 62 (2014) 161–171, https://doi.org/10.1016/J.OPTLASTEC.2014.03.008.
[61] M. Gustafsson, M. Thuvander, E.L. Bergqvist, E. Keehan, L. Karlsson, Effect of welding procedure on texture and strength of nickel based weld metal, Sci. Technol. Weld. Join. 12 (2013) 549–555, https://doi.org/10.1179/174329307X213800.
[62] M. Gäumann, S. Henry, F. Cléton, J.D. Wagnière, W. Kurz, Epitaxial laser metal forming: analysis of microstructure formation, Mater. Sci. Eng. A 271 (1999) 232–241, https://doi.org/10.1016/S0921-5093(99)00202-6.
[63] H.T. Liu, Z.Y. Liu, Y.Q. Qiu, G.M. Cao, C.G. Li, G.D. Wang, Characterization of the solidification structure and texture development of ferritic stainless steel produced by twin-roll strip casting, Mater. Charact. 60 (2009) 79–82, https://doi.org/10.1016/J.MATCHAR.2008.06.005.
[64] F. Fang, Y.X. Zhang, X. Lu, Y. Wang, M.F. Lan, G. Yuan, R.D.K. Misra, G.D. Wang, Abnormal growth of {100} grains and strong Cube texture in strip cast Fe-Si electrical steel, Scr. Mater. 147 (2018) 33–36, https://doi.org/10.1016/J.SCRIPTAMAT.2017.12.034.
[65] M. Mukherjee, S. Saha, T.K. Pal, P. Kanjilal, Influence of modes of metal transfer on grain structure and direction of grain growth in low nickel austenitic stainless steel weld metals, Mater. Charact. 102 (2015) 9–18, https://doi.org/10.1016/J.MATCHAR.2015.02.006.
[66] S. Kou, Welding Metallurgy, third ed., Wiley, 2021 https://doi.org/10.1002/0471434027.
[67] Y. Liu, J. Shi, Epitaxial growth and stray grain control toward single-crystal metallic materials by additive manufacturing: a review, Adv. Eng. Mater. 25 (2023), https://doi.org/10.1002/adem.202201917.
[68] F. Schmeiser, E. Krohmer, C. Wagner, N. Schell, E. Uhlmann, W. Reimers, In situ microstructure analysis of Inconel 625 during laser powder bed fusion, J. Mater. Sci. 57 (2021) 9663–9677, https://doi.org/10.1007/s10853-021-06577-8.
[69] B. Lan, Y. Wang, Y. Liu, P. Hooper, C. Hopper, G. Zhang, X. Zhang, J. Jiang, The influence of microstructural anisotropy on the hot deformation of wire arc additive manufactured (WAAM) inconel 718, Mater. Sci. Eng. A 823 (2021) 141733, https://doi.org/10.1016/j.msea.2021.141733.
[70] K. Zhang, B. Holmedal, T. Mánik, A. Saai, Assessment of advanced Taylor models, the Taylor factor and yield-surface exponent for FCC metals, Int. J. Plast. 114 (2019) 144–160, https://doi.org/10.1016/j.ijplas.2018.10.015.
[71] W.F. Hosford, The Mechanics of Crystals and Textured Polycrystals, first ed., Oxford University Press, 1993.
[72] G.E. Dieter, D. Bacon, Mechanical Metallurgy, third ed., McGraw-Hill, New York, 1976.
[73] H.L. Wei, J. Mazumder, T. DebRoy, Evolution of solidification texture during additive manufacturing, Sci. Rep. 5 (2015) 16446, https://doi.org/10.1038/srep16446.
[74] L. Thijs, M.L. Montero Sistiaga, R. Wauthle, Q. Xie, J.-P. Kruth, J. Van Humbeeck, Strong morphological and crystallographic texture and resulting yield strength anisotropy in selective laser melted tantalum, Acta Mater. 61 (2013) 4657–4668, https://doi.org/10.1016/j.actamat.2013.04.036.
[75] T.M. Smith, N.M. Senanayake, C.K. Sudbrack, P. Bonacuse, R.B. Rogers, P. Chao, J. Carter, Characterization of nanoscale precipitates in superalloy 718 using high resolution SEM imaging, Mater. Charact. 148 (2019) 178–187, https://doi.org/10.1016/j.matchar.2018.12.018.
[76] V.V. Rielli, A. Piglione, M.-S. Pham, S. Primig, On the detailed morphological and chemical evolution of phases during laser powder bed fusion and common post-processing heat treatments of IN718, Addit. Manuf. 50 (2022) 102540, https://doi.org/10.1016/j.addma.2021.102540.
[77] R. Cozar, A. Pineau, Morphology of γ' and γ" precipitates and thermal stability of inconel 718 type alloys, Metall. Trans. 4 (1973) 47–59, https://doi.org/10.1007/BF02649604.
[78] W.T. Geng, D.H. Ping, Y.F. Gu, C.Y. Cui, H. Harada, Stability of nanoscale co-precipitates in a superalloy: a combined first-principles and atom probe tomography study, Phys. Rev. B 76 (2007) 224102, https://doi.org/10.1103/PhysRevB.76.224102.
[79] S.L. Semiatin, N.C. Levkulich, R. Larsen, J.S. Tiley, K.N. Wertz, F. Zhang, T. M. Smith, R.Y. Zhang, H.B. Dong, P. Gadaud, J. Cormier, The application of differential scanning calorimetry to investigate precipitation behavior in nickel-base superalloys under continuous cooling and heating conditions, Metall. Mater. Trans. A. 52 (2021) 3706–3726, https://doi.org/10.1007/s11661-021-06362-x.
[80] R. Shi, D.P. McAllister, N. Zhou, A.J. Detor, R. DiDomizio, M.J. Mills, Y. Wang, Growth behavior of γ'/γ'' coprecipitates in Ni-Base superalloys, Acta Mater. 164 (2019) 220–236, https://doi.org/10.1016/j.actamat.2018.10.028.
[81] V.V. Rielli, F. Theska, F. Godor, A. Stanojevic, B. Oberwinkler, S. Primig, Evolution of nanoscale precipitates during common Alloy 718 ageing treatments, Mater. Des. 205 (2021) 109762, https://doi.org/10.1016/j.matdes.2021.109762.
[82] C. Slama, M. Abdellaoui, Structural characterization of the aged Inconel 718, J. Alloys Compd. 306 (2000) 277–284, https://doi.org/10.1016/S0925-8388(00)00789-1.
[83] A. Devaux, L. Nazé, R. Molins, A. Pineau, A. Organista, J.Y. Guédou, J.F. Uginet, P. Héritier, Gamma double prime precipitation kinetic in Alloy 718, Mater. Sci. Eng. A 486 (2008) 117–122, https://doi.org/10.1016/j.msea.2007.08.046.
[84] Z. Li, X. Ma, C. Zhong, S. Sui, A. Gasser, J. Chen, Microstructure homogeneity and mechanical property improvement of Inconel 718 alloy fabricated by high-deposition-rate laser directed energy deposition, Mater. Sci. Eng. A 832 (2022) 142430, https://doi.org/10.1016/j.msea.2021.142430.
[85] T.L. Anderson, Fracture Mechanics, Fourth, CRC Press, 2017, https://doi.org/10.1201/9781315370293.
[86] C.E. Seow, J. Zhang, H.E. Coules, G. Wu, C. Jones, J. Ding, S. Williams, Effect of crack-like defects on the fracture behaviour of Wire + Arc Additively Manufactured nickel-base alloy 718, Addit. Manuf. 36 (2020) 101578, https://doi.org/10.1016/j.addma.2020.101578.
[87] T.L. Johnston, C.E. Feltner, Grain size effects in the strain hardening of polycrystals, Metall. Trans. 1 (1970) 1161–1167, https://doi.org/10.1007/BF02900226.
[88] Y.-T. Chen, A.-C. Yeh, M.-Y. Li, S.-M. Kuo, Effects of processing routes on room temperature tensile strength and elongation for Inconel 718, Mater. Des. 119 (2017) 235–243, https://doi.org/10.1016/j.matdes.2017.01.069.
[89] I.S. Yasnikov, A. Vinogradov, Y. Estrin, Revisiting the Considère criterion from the viewpoint of dislocation theory fundamentals, Scr. Mater. 76 (2014) 37–40, https://doi.org/10.1016/j.scriptamat.2013.12.009.
[90] N. Xi, Z. Ni, X. Fang, Y. Zhou, K. Tang, H. Zhang, K. Huang, Role of δ-phase on mechanical behaviors of additive Manufactured Inconel 718: detailed microstructure analysis and crystal plasticity modelling, Int. J. Plast. 168 (2023) 103708, https://doi.org/10.1016/j.ijplas.2023.103708.

[91] Q. Chen, G. Wang, H. Zhang, R. Li, Research on microstructure and mechanical properties of hybrid plasma arc and micro-rolling additive manufacturing of Inconel 718 superalloy, Rapid Prototyp. J. 28 (2022) 1509–1519, https://doi.org/10.1108/rpj-09-2021-0227.

[92] K. Wang, Y. Liu, Z. Sun, J. Lin, Y. Lv, B. Xu, Microstructural evolution and mechanical properties of Inconel 718 superalloy thin wall fabricated by pulsed plasma arc additive manufacturing, J. Alloys Compd. 819 (2020) 152936, https://doi.org/10.1016/J.JALLCOM.2019.152936.

[93] W.S. James, S. Ganguly, G. Pardal, High temperature performance of wire-arc additive manufactured Inconel 718, Sci. Rep. 13 (2023) 1–7, https://doi.org/10.1038/s41598-023-29026-9.

[94] C. Keller, E. Hug, X. Feaugas, Microstructural size effects on mechanical properties of high purity nickel, Int. J. Plast. 27 (2011) 635–654, https://doi.org/10.1016/j.ijplas.2010.08.002.

[95] U.F. Kocks, H. Mecking, Physics and phenomenology of strain hardening: the FCC case, Prog. Mater. Sci. 48 (2003) 171–273, https://doi.org/10.1016/S0079-6425(02)00003-8.

[96] C. Keller, E. Hug, Kocks-Mecking analysis of the size effects on the mechanical behavior of nickel polycrystals, Int. J. Plast. 98 (2017) 106–122, https://doi.org/10.1016/j.ijplas.2017.07.003.

[97] M.F. Ashby, The deformation of plastically non-homogeneous materials, Philos. Mag. A J. Theor. Exp. Appl. Phys. 21 (1970) 399–424, https://doi.org/10.1080/14786437008238426.

[98] K.V.U. Praveen, G.V.S. Sastry, V. Singh, Work-Hardening behavior of the Ni-Fe based superalloy IN718, Metall. Mater. Trans. A. 39 (2008) 65–78, https://doi.org/10.1007/s11661-007-9375-3.

[99] S. Li, J.Y. Li, Z.W. Jiang, Y. Cheng, Y.Z. Li, S. Tang, J.Z. Leng, H.X. Chen, Y. Zou, Y.H. Zhao, J.P. Oliveira, Y. Zhang, K.H. Wang, Controlling the columnar-to-equiaxed transition during directed energy deposition of Inconel 625, Addit. Manuf. 57 (2022) 102958, https://doi.org/10.1016/j.addma.2022.102958.

[100] Y. Kok, X.P.P. Tan, P. Wang, M.L.S.L.S. Nai, N.H.H. Loh, E. Liu, S.B.B. Tor, Anisotropy and heterogeneity of microstructure and mechanical properties in metal additive manufacturing: a critical review, Mater. Des. 139 (2018) 565–586, https://doi.org/10.1016/j.matdes.2017.11.021.

[101] S. Dixit, S. Liu, H.A. Murdoch, P.M. Smith, Investigating build orientation-induced mechanical anisotropy in additive manufacturing 316L stainless steel, Mater. Sci. Eng. A 880 (2023) 145308, https://doi.org/10.1016/j.msea.2023.145308.

[102] T. Hassel, T. Carstensen, Properties and anisotropy behaviour of a nickel base alloy material produced by robot-based wire and arc additive manufacturing, Weld. World 64 (2020) 1921–1931, https://doi.org/10.1007/s40194-020-00971-7.

[103] E. Hosseini, V.A. Popovich, A review of mechanical properties of additively manufactured Inconel 718, Addit. Manuf. 30 (2019) 100877, https://doi.org/10.1016/j.addma.2019.100877.

[104] D.M. Dimiduk, M.D. Uchic, T.A. Parthasarathy, Size-affected single-slip behavior of pure nickel microcrystals, Acta Mater. 53 (2005) 4065–4077, https://doi.org/10.1016/j.actamat.2005.05.023.

[105] R.W.W. Kozar, A. Suzuki, W.W.W. Milligan, J.J.J. Schirra, M.F.F. Savage, T.M. M. Pollock, Strengthening mechanisms in polycrystalline multimodal nickel-base superalloys, Metall. Mater. Trans. A. 40 (2009) 1588–1603, https://doi.org/10.1007/s11661-009-9858-5.

[106] E.I. Galindo-Nava, L.D. Connor, C.M.F. Rae, On the prediction of the yield stress of unimodal and multimodal γ′ nickel-base superalloys, Acta Mater. 98 (2015) 377–390, https://doi.org/10.1016/j.actamat.2015.07.048.

[107] G.K. Williamson, W.H. Hall, X-ray line broadening from filed aluminium and wolfram, Acta Metall. 1 (1953) 22–31, https://doi.org/10.1016/0001-6160(53)90006-6.

[108] R.E. Smallman, K.H. Westmacott, Stacking faults in face-centred cubic metals and alloys, Philos. Mag. A J. Theor. Exp. Appl. Phys. 2 (2010) 669–683, https://doi.org/10.1080/14786435708242709.

[109] A. Arsenlis, D. Parks, Crystallographic aspects of geometrically-necessary and statistically-stored dislocation density, Acta Mater. 47 (1999) 1597–1611, https://doi.org/10.1016/S1359-6454(99)00020-8.

[110] A. Borbély, The modified Williamson-Hall plot and dislocation density evaluation from diffraction peaks, Scr. Mater. 217 (2022) 114768, https://doi.org/10.1016/j.scriptamat.2022.114768.

[111] S.K. Rai, A. Kumar, V. Shankar, T. Jayakumar, K.B.S. Rao, B. Raj, Characterization of microstructures in Inconel 625 using X-ray diffraction peak broadening and lattice parameter measurements, Scr. Mater. 51 (2004) 59–63, https://doi.org/10.1016/J.SCRIPTAMAT.2004.03.017.

[112] J.E. Bailey, P.B. Hirsch, The dislocation distribution, flow stress, and stored energy in cold-worked polycrystalline silver, Philos. Mag. A J. Theor. Exp. Appl. Phys. 5 (2006) 485–497, https://doi.org/10.1080/14786436008238300.

[113] B. Reppich, Some new aspects concerning particle hardening mechanisms in γ' precipitating Ni-base alloys—I. Theoretical concept, Acta Metall. 30 (1982) 87–94, https://doi.org/10.1016/0001-6160(82)90048-7.

[114] F. Brenne, A. Taube, M. Pröbstle, S. Neumeier, D. Schwarze, M. Schaper, T. Niendorf, Microstructural design of Ni-base alloys for high-temperature applications: impact of heat treatment on microstructure and mechanical properties after selective laser melting, Prog. Addit. Manuf. 1 (2016) 141–151, https://doi.org/10.1007/s40964-016-0013-8.

[115] F. Chen, Q. Wang, C. Zhang, Z. Huang, M. Jia, Q. Shen, Microstructures and mechanical behaviors of additive manufactured Inconel 625 alloys via selective laser melting and laser engineered net shaping, J. Alloys Compd. 917 (2022) 165572, https://doi.org/10.1016/j.jallcom.2022.165572.

[116] X. Yao, Q. Ding, X. Zhao, X. Wei, J. Wang, Z. Zhang, H. Bei, Microstructural rejuvenation in a Ni-based single crystal superalloy, Mater. Today Nano 17 (2022) 100152, https://doi.org/10.1016/j.mtnano.2021.100152.

[117] L.A. Gypen, A. Deruyttere, Multi-component solid solution hardening, J. Mater. Sci. 12 (1977) 1028–1033, https://doi.org/10.1007/BF00540987.

[118] V.T. Le, D.S. Mai, T.K. Doan, H. Paris, Wire and arc additive manufacturing of 308L stainless steel components: optimization of processing parameters and material properties, Eng. Sci. Technol. an Int. J. 24 (2021) 1015–1026, https://doi.org/10.1016/J.JESTCH.2021.01.009.

[119] B. Wu, Z. Pan, S. Li, D. Cuiuri, D. Ding, H. Li, The anisotropic corrosion behaviour of wire arc additive manufactured Ti-6Al-4V alloy in 3.5% NaCl solution, Corros. Sci. 137 (2018) 176–183, https://doi.org/10.1016/J.CORSCI.2018.03.047.

[120] Y. Xie, M. Gao, F. Wang, C. Zhang, K. Hao, H. Wang, X. Zeng, Anisotropy of fatigue crack growth in wire arc additive manufactured Ti-6Al-4V, Mater. Sci. Eng. A 709 (2018) 265–269, https://doi.org/10.1016/J.MSEA.2017.10.064.

[121] T. Vilaro, C. Colin, J.-D. Bartout, L. Nazé, M. Sennour, Microstructural and mechanical approaches of the selective laser melting process applied to a nickel-base superalloy, Mater. Sci. Eng. A 534 (2012) 446–451, https://doi.org/10.1016/j.msea.2011.11.092.

[122] H.A. Roth, C.L. Davis, R.C. Thomson, Modeling solid solution strengthening in nickel alloys, Metall. Mater. Trans. A. 28 (1997) 1329–1335, https://doi.org/10.1007/s11661-997-0268-2.

[123] M. Preuss, J.Q. da Fonseca, B. Grant, E. Knoche, R. Moat, D. Mark, The effect of γ′ particle size on the deformation mechanism in an advanced polycrystalline nickel-base superalloy, in: Superalloys 2008, 2008, pp. 405–414.

[124] M. Huang, Z. Li, J. Tong, The influence of dislocation climb on the mechanical behavior of polycrystals and grain size effect at elevated temperature, Int. J. Plast. 61 (2014) 112–127, https://doi.org/10.1016/j.ijplas.2014.06.002.

[125] P. Zhang, Y. Yuan, B. Li, S.W. Guo, G.X. Yang, X.L. Song, Tensile deformation behavior of a new Ni-base superalloy at room temperature, Mater. Sci. Eng. A 655 (2016) 152–159, https://doi.org/10.1016/j.msea.2015.12.089.

[126] P.M. Kelly, The effect of particle shape on dispersion hardening, Scr. Metall. 6 (1972) 647–656, https://doi.org/10.1016/0036-9748(72)90120-2.

[127] E. Farabi, V.V. Rielli, F. Godor, C. Gruber, A. Stanojevic, B. Oberwinkler, S. P. Ringer, S. Primig, Advancing structure – property homogeneity in forged Alloy 718 engine disks: a pathway towards enhanced performance, Mater. Des. 242 (2024) 112987, https://doi.org/10.1016/j.matdes.2024.112987.

[128] J.M. Oblak, D.S. Duvall, D.F. Paulonis, An estimate of the strengthening arising from coherent, tetragonally-distorted particles, Mater. Sci. Eng. 13 (1974) 51–56, https://doi.org/10.1016/0025-5416(74)90020-2.

[129] J.M. Oblak, D.F. Paulonis, D.S. Duvall, Coherency strengthening in Ni base alloys hardened by DO22 γ′ precipitates, Metall. Trans. 5 (1974) 143–153, https://doi.org/10.1007/BF02642938.

[130] S.P. Yuan, G. Liu, R.H. Wang, X. Pu, G.-J. Zhang, J. Sun, K.-H. Chen, Coupling effect of multiple precipitates on the ductile fracture of aged Al–Mg–Si alloys, Scr. Mater. 57 (2007) 865–868, https://doi.org/10.1016/j.scriptamat.2007.06.063.

[131] B. Wahlmann, M. Markl, C. Körner, A thermo-mechanical model for hot cracking susceptibility in electron beam powder bed fusion of Ni-base superalloys, Mater. Des. 237 (2024) 112528, https://doi.org/10.1016/j.matdes.2023.112528.

[132] T.A. Rodrigues, V.R. Duarte, D. Tomás, J.A. Avila, J.D. Escobar, E. Rossinyol, N. Schell, T.G. Santos, J.P. Oliveira, In-situ strengthening of a high strength low alloy steel during wire and Arc Additive Manufacturing (WAAM), Addit. Manuf. 34 (2020) 101200, https://doi.org/10.1016/j.addma.2020.101200.